Stony Brook University

A greedy method to simulate drainage in cross sections

A Dissertation presented

by

Long Li

to

The Graduate School

in Partial Fulfillment of the

Requirements

for the Degree of

Doctor of Philosophy

in

Applied Mathematics and Statistics

(Computational Applied Mathematics)

Stony Brook University

August 2014

Stony Brook University

The Graduate School

Long Li

We, the dissertation committe for the above candidate for the

Doctor of Philosophy degree, hereby recommend

acceptance of this dissertation

W. Brent Lindquist - Dissertation Advisor
Professor of Department of Applied Mathematics and Statistics

Xiaolin Li - Chairperson of Defense
Professor of Department of Applied Mathematics and Statistics

Roman Samulyak - Committee Member
Professor of Department of Applied Mathematics and Statistics

Alexander Orlov - Outside Member
Associate Professor of Department of Materials Science and Engineering

This dissertation is accepted by the Graduate School

Charles Taber
Dean of the Graduate School

Abstract of the Dissertation

A greedy method to simulate drainage in cross sections

by

Long Li

Doctor of Philosophy

in

Applied Mathematics and Statistics

(Computational Applied Mathematics)

Stony Brook University

2014

Porous media, such as rocks and soil, make up the largest proportion of mass in nature. Pore-network model is a widely used model to describe the tiny and complicated inner structure of porous media. Assisted by the development of X-ray computed microtomography in recent years, researchers are able to extract the geometric characters of inner pores and throats from porous media, then further explore two-phase flow in porous media more exactly. Drainage, a process that a non-wetting phase fluid replaces the other wetting fluid, is the research topic of this thesis. The boundaries between two different phases, named as menisci consisting of arcs with same radii, are formed by surface tension between two phases. A greedy-type method is presented to calculate the arc-meniscus at entry pressure for drainage into the cross section of an infinitely long capillary tube under arbitrary wetting angle in the range $[0, \pi/2)$. By the greedy method we construct counterclockwise(CC) circuits which represent the different non-wetting regions, then the entry radius of a cross section could be achieved by comparing different entry radii of the corresponding CC-circuits. In addition, we can also extract the drainage axis of a polygon with a wetting angle in the range $[0, \pi/2)$ by

the greedy method. We obtain the entry radii from 23,639 throat polygons derived from the 3D analysis of tomography images of a Fontainebleau sandstone sample having 22% porosity. Then we derive an empirical formula, which considers the effects of area A, perimeter P, wetting angle θ and the number of polygon edges n, to estimate the entry radius for any arbitrary polygon. With the simplification of the formula, our results also show that the ratio, $A/(P \cdot \cos\theta)$, is a good estimator of the entry radius within 5% error on average for Fontainebleau samples.

Table of Contents

List of Figures

List of Tables

Acknowledgements

Thanks to my advisor, Prof. W. Brent Lindquist who leads me to the wonderland of research, and his instruction during my research. This thesis also benefits from the suggestions of my committee: Prof. Xiaolin Li, Prof. Roman Samulyak and Prof. Alexander Orlov.

During my research Prof. Xiangmin Jiao and Prof. Jiaqiao Hu gave me some precious suggestions on numerical analysis and statistics respectively. In addition, I want to thank my English tutors, Ted Ginsberg and Martha Fink. Their generous help improves my language skill greatly. My labmates, Dr. Daesang Kim, Kyungtak, Seunghee and Joowon never hesitate to lend hands to me when I need them.

No words can express my appreciation for my dear parents, Enzhi and Weicai, as well my Big Brother Yibing. Without their love and encouragement I can't enjoy the pleasure of the exploration.

Last but not least, I owe a lot to my wife Xiaolu during the preparation of this thesis, I am not able to finish it without her endless support.

1 Introduction

Porous media are the most widespread substances in nature. A porous medium is a material holding pores (empty space) inside. Many natural materials such as soil, rocks, biological tissues, and some man-made stuff like cements are also considered as porous media [1].

The definition of two phase flow varies in different research fields, in our research two phase flow refers to a mixture of two different fluids with distinct wetting phase. The boundary between two different phases is named as meniscus which is formed by surface tension.

Ordinary as they are, porous media usually have extremely complicated inner topological structure, which leads to a tough task to study the two phase flow in porous media. Our research is focused on one part of it - drainage process. Our simulation is to calculate the entry radius of menisci, which corresponds to the minimum pressure to push a non-wetting fluid into an infinitely long capillary tube with constant polygonal cross section which is previously occupied by the other wetting fluid. Our research goals are:

1. Design a method to calculate exactly the entry radius of drainage process for arbitrary polygonal cross section under a wetting angle in $[0, \pi/2)$;

2. Summarize our results into an empirical formula to predict the entry radius for any arbitrary polygon under a wetting angle in $[0, \pi/2)$.

The cross sections used in our study derived from 3D analysis of an X-ray computed microtomographic (XCMT) [33] image of a 22% porosity

Fontainebleau sandstone sample with volume $3.14 \times 3.14 \times 3.14 mm^3$ imaged at 5.7 μm voxel size.

1.1 Pore network model

In 1950s some simple models were proposed [6, 7] to study the capillary flow in porous media. Those models suggest that porous media are consisted of a group of parallel capillary tubes, and pores are the empty space between the tubes. The flaw of those models is they ignore an important feature about porous media: pores are interconnected with each other. However, those simple models make it easier to study capillary phenomena by experiment, and those early experiments [46, 47, 48] built a base for the later research.

In 1956 a novel model named pore network model appeared. Represented by Fatt [11, 12, 13], it has been a widely used model to describe the inner structure of porous media since then. In this model a pore is connected with its neighbors by the channels and the cross section with the minimum area is called throat.

Constricted by the complex inner structure of porous media, the early researchers employed a simplified pore network model to study the flow in porous media. For example, pores are idealized as spheres or cylinders and throats as circles [9, 10, 25, 26]. However, this simplification only works for single phase flow. Leaving no space for corner flow which was studied by experiment [30], this idealization is unfit for two phase or multi-phase flow.

To accommodate the corner flow in pores and throats, Mason and Morrow

[41] proposed irregular triangle to represent the cross section of pores and throat. As an irregular triangle could be adjusted by shape factor A/P^2, where A is area and P is perimeter, this simplification offers more flexibility to the model. ren et al. [44] adopted this idea to study Bentheimer sandstone same, finding that this model can predict capillary pressure and relative permeability very well.

Similarly Fenwick and Blunt [14, 15] chose square cross sections for pores and throats. Other researchers even went further. Man and Jing [38, 39, 40] created a star-like grain boundary pore (GBP) shape to describe throats. Moreover, a polygon consisting of three acute angles is constructed by van Dijke et al. [52] to represent the pore cross sections.

In sum, various of idealized pores and throats were proposed to simplify the pore network model, however, those simplified models only work for some special cases. This problem is partially caused by the complicated inner structure of porous media which researcher can't achieve until the development of X-ray computed microtomography (XCMT).

XCMT, a non-destructive image process method, can leverage three dimensional data from which three dimensional images could be extracted [16, 23]. This technology was soon combined with pore network model to explore the inner structure of porous media [51, 31, 32, 33]. Based on the previous work, a software package named 3DMA was developed to extract XCMT images and analyze pore network [34]. To get the throat samples by 3DMA, three steps was executed in order:

a) Segmentation. This step is to separate voxels into grain and pores, utilizing indicator-kriging algorithm [43];

b) Construction of media axis (MA). 3DMA code uses the algorithm of Lee-Kashyap and Chu [29] to construct MA paths;

c) Throat construction. Several different algorithm are employed to extract throats from MA paths and pore boundaries [35, 49, 50].

1.2 Primary drainage in a polygonal cross section

Throats play a critical role in the drainage process. Throats locally control the advance of the invading fluid front, determining the minimum capillary pressure needed to advance the non-wetting fluid through each channel [11]. This minimal pressure, referred to as the entry pressure, is determined by the geometry of the throat and by surface tensions. Except for circular cross sectional shapes, the movement of the non-wetting fluid through a channel is accompanied by the formation of films of (residual) wetting fluid separated from the (invading) non-wetting fluid by arc menisci. The residual film formation (which qualitatively clings in the sharp corners of the cross section) is determined at entry. The film configuration evolves under increase in capillary pressure; the arc menisci are driven further into corners and the wetting films become thinner. For a two phase flow of oil and water, Kovscek et al. [27] verified that in drainage process the pore boundaries enclosing the oil phase which occupied the pore center were oil-wet, which had been water-wet before the drainage. And the boundaries surrounding the water phase

still kept water-wet.

For an infinitely long capillary tube of constant cross section, the entry pressure condition under quasi-static flow was derived by Mayer, Stowe and Princen (MS-P) [42, 46, 47, 48] by considering force equilibrium and change in free energy. MS-P theory has been applied analytically in cross sections of regular polygons[28, 37]. For a perfectly wetting fluid ($\theta = 0°$) Lindquist [36] showed that, under the conditions of MS-P theory, the center of curvature of every arc meniscus must always remain on medial axis (MA) [3] of the cross section. The existence of a continuous radius function defined along the medial axis makes it possible to solve MS-P equation for the entry pressure and arc menisci configuration. Evolution of the arc menisci under subsequent increase in capillary pressure is determined completely by the arc menisci movement along the "centrifugal" portion of the medial axis [36]. Using the medial axis, Held [20] developed an analytic solution for the radius and configuration of arc-menisci at entry pressure for convex polygons, again under the restriction of 0° wetting angle. Lindquist [36] further showed that a one-parameter family of axes, $DA(\theta)$, referred to as drainage axes (DA) governed the movement of arc menisci centers of curvature in the case of non-zero wetting angles. ($D(\theta = 0°)$ is identical to the medial axis.)

Glantz and Hilpert [18] introduced the chordal axis (CA) which determined the movement of the center point of each meniscus chord (the chord which joins the two end-points of an arc meniscus). They developed an analytic technique to construct the CA for the case $\theta = 0°$. Unlike the medial

axis, the CA does not form a connected structure inside the cross section. And they were able to postulate a method to connect the CA through "forbidden" triangular regions which the chords cannot enter. Both chord and drainage axes also govern arc meniscus motion during imbibition. Kim and Lindquist [24] developed a numerical method to compute the evolving arc menisci configuration during imbibition. They demonstrate by construction that, for a given cross section, a single CA exists which governs movement of the center point of any meniscus chord for all wetting angles in the range $\theta \in [0, \pi/2)$. For a fixed wetting angle only a portion of the CA is relevant for meniscus movement. They also confirm the $\theta = 0^\circ$ CA construction by Glantz and Hilpert outside of the "forbidden" regions. However, for $\theta > 0$, chords do in fact enter these "forbidden" regions and that the "connection" method postulated by Glantz and Hilpert fails for $\theta > 0$. Thus we are currently left with numerical methods to compute arc meniscus configurations for most cross sectional shapes.

Frette and Helland [17, 21] have developed a numerical method to compute the entry pressure/arc-menisci configuration in cross sections from digitized images for arbitrary wetting angle in $[0, \pi/2)$. The method works on a pixel discretization of the cross section. For a fixed radius, all potential arc-menisci are computed. In subsequent steps, irrelevant arc-menisci are detected and deleted and in the case of multiple non-wetting fluid regions, the non-wetting fluid regions are identified. These steps are repeated, changing the radius until the arc-meniscus configuration converges to a solution of the

Mayer-Stowe entry condition. It is currently the only available method which handles cross sections which support multiple non-wetting fluid regions.

In this thesis a numerical approach is developed to locate arc menisci during drainage, finding both the entry pressure configuration as well as configurations at arbitrary capillary pressure (whether realized or not during drainage). Unlike the Frette-Helland method, the method utilizes an polygon edge-vertex description of the cross section perimeter. This offers an advantage in reducing the computational burden of the algorithm. We characterize our algorithm as "greedy" in the sense that it constructs a global solution by making a local choice at each stage of construction. The method is described in section 2.

An important consideration, particularly for modern multiphase network flow models [2, 4], is the ability to rapidly compute accurate entry pressures and fluid films. Frette and Helland [17] propose the approximation

$$r_e = \frac{A}{L}\frac{f(\theta)}{\cos\theta}, \tag{1}$$

where A and L are the area and perimeter of the cross section, and $f(\theta)$ is a functional form to be determined. This is an extension of the "hydraulic radius" $r_H = A/L$ proposed by Hwang [22]. Based upon an analysis of 70 pore spaces in Bentheimer sandstone (2D SEM, 1.28 μm resolution) using their numerical method, Frette and Holland provide the estimates $f(0^\circ) = 1.35,$, $f(40^\circ) = 1.22$. In section 3 we apply our algorithm to a data set of

23,639 throat polygons to determine a more complete analysis of the form of $f(\theta)$.

In the last section we summarize the greedy method and the result we achieve, we also discuss some future research which could be derived from our current work.

2 Simulation method

2.1 Mathematics model

The Mayer-Stowe-Princen (MS-P) condition [42, 46, 47, 48] for the entry pressure P_C^e can be written

$$P_C^e = \frac{(\sigma_{NS} - \sigma_{WS})\, L_{NS} + \sigma_{NW}\, L_{NW}}{A_N}, \tag{2}$$

where σ, L, and A refer to surface tension, inter-phase contact length, and area. The subscripts N, W, and S denote non-wetting, wetting, and solid phases. Thus, in Eq.(2), L_{NS} is the length of the perimeter over which the solid contacts with the non-wetting fluid, L_{NW} is the total interface length between the two different fluids, and A_N is the area of the non-wetting fluid. Using the form of the Young-Laplace condition appropriate to this geometry,

$$P_C^e = \frac{\sigma_{NW}}{r_e}, \tag{3}$$

which relates the entry pressure to the common radius of curvature r_e of all arc menisci formed in the cross section at entry, Eq.(2) can be written [36]

$$2r_e^2 \sum_i \alpha_i + r_e \cos\theta\, L_{NS}(r_e) - A_N(r_e) = 0, \tag{4}$$

where the sum is over all arc menisci, α_i is one half of the opening angle of arc meniscus i, and θ is the wetting angle. Fig.1 illustrates the corresponding

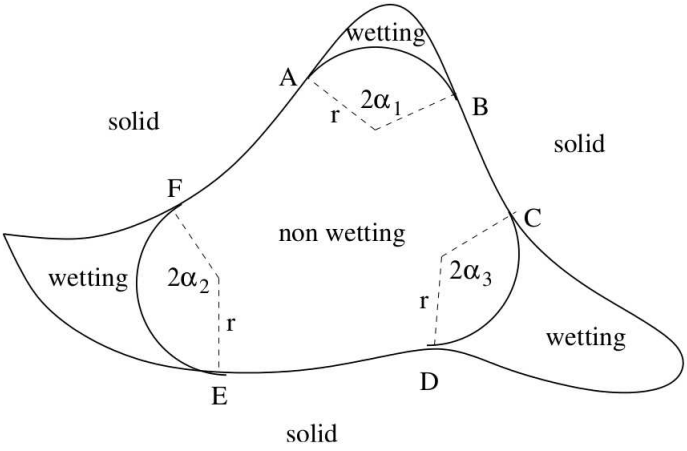

Figure 1: Illustration of drainage in a capillary tube [36].

variables in Eq.(4).

Eq.(4) is the governing equation of our research, and it is not a simple rewriting of Eq.(2), the MSP equation. Note that MSP equation consists of pressure and surface tension which are physics quantities, thus MSP is definitely a physical equation. While Eq.(4) is composed of radius, angle, length and area, and all of those are geometry quantities, therefore Eq.(4) is a geometry equation. So Eq.(4) transforms a physics problem into a geometry problem, and the bridge between them is Eq.(3), Young-Laplace equation. As a result, the entry pressure and entry radius are equivalent, and our research will focus on a geometry problem - how to find the entry radius.

To achieve this goal we must solve the non-linear quadratic Eq.(4) whose coefficient, α, L and A, are decided by radius r. In other words, for a given r the function value is determined by the location of the corresponding menisci

which is illustrated in Fig.1, consequently, we concentrate on how to locate the menisci for a given radius r.

2.2 Greedy method

Medial axis(MA) matches with the drainage axis (DA) when the wetting angle is 0° [36]. Based on Eq.(4), entry menisci could be found along MA if the cross section holds only one single non-wetting region. Fig.2 shows the location of entry menisci in 16 cross section samples. However, although Voronoi algorithm can calculate MA efficiently [45], DA deforms when the wetting angle is greater than 0°, and doesn't coincide with MA any more.

The above idea is to locate the entry menisci in a "from-top-to-bottom" way, as MA is a global geometry character of a polygon. Now we are trying to solve this problem in another direction - " from-bottom-to-top" .

From Fig.2 we observe that all of the menisci lie on the corners of polygons, far from the center of maximum inscribed circles (MIC). Thus, if we can find the corresponding menisci for the corners individually and concatenate them together, then we get the results same with Fig.2.

This idea derives from the greedy method [8]. When the global optimal solution is too hard to be found, the greedy method tries to look for a local optimal solution for one part of the problem, and repeat this process until the whole problem is dissolved, then the collection of the local optimal solutions should be the global optimal solution if the problem satisfies the requirement for the greedy method. A classic example to explain the greedy method is a

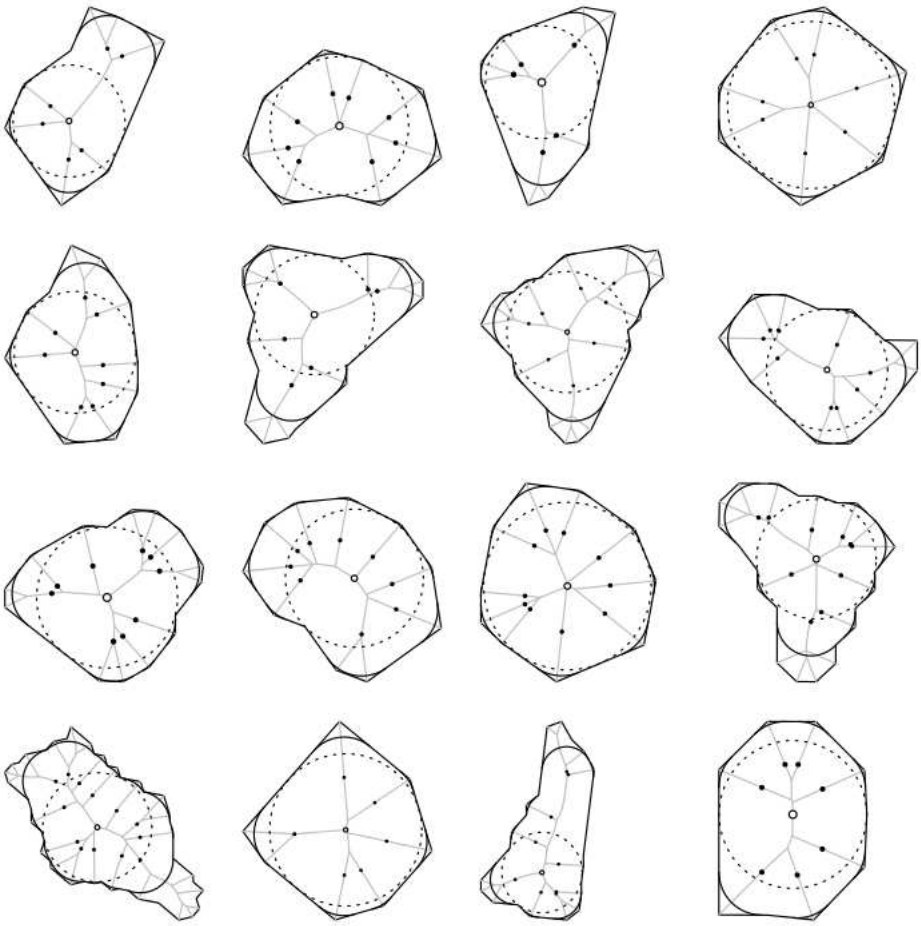

Figure 2: Illustration of entry menisci of 16 sample cross sections [36]. Light grey lines are MA, dark arcs are the entry menisci, solid points are their centers and empty points denote centers of maximum inscribed circles (MIC).

	Coins	Left Problem
Quarter	3	21
Dime	2	1
Cent	1	0

Table 1: An example of change-making problem.

Corners	Meniscus
1	M_1
$\vdots$	$\vdots$
n	M_n

Table 2: The idea to locate all of entry menisci in corresponding corners.

change-making problem. One instance of the problem is: how to express 96 cents with the least amount of coins by quarter, dime and cent?

This problem is solved in three steps shown in Table 1. In each step only the local optimal solution is found, and the problem is shrinking to a smaller one. The collection of the three local optimal solutions is the global optimal solution we are looking for. Our idea to locate the menisci, shown in Table 2, is analogous to this procedure.

For a given corner, after we find the corresponding meniscus, we can switch to the next neighbor corner and look for its meniscus. Repeat this process until we traverse all of the corners. To implement this idea we must face two questions regarding to the row and the column of Table 2.

1) How to find the corresponding meniscus for a given corner?

2) After the meniscus of a corner is detected, how to switch to its neighbor

corner?

We design a counterclockwise(CC) circuit with double loops to answer the two answers. The inner loop is responsible to discover the correct meniscus of a corner, as well the outer loop is to concatenate all of the menisci together. The following parts will give more details about the CC circuit.

2.3 Preliminaries

We work within the class of polygons in the plane whose interiors are simply connected. For any polygon in this class, arbitrarily choose one of the two normal directions to the plane to be the positive normal $\overrightarrow{n}$. We number the edges clockwise, relative to $\overrightarrow{n}$, sequentially from E_1 to E_n starting from an arbitrary edge. Vertices are also numbered sequentially clockwise, inheriting their numbering from the edges; vertex V_{i+1} lies between edges E_i andE_{i+1}. (Vertex V_1 lies between E_n and E_1.) We refer to the edges and vertices of the polygon as perimeter "components".

In 2D, as each arc meniscus is the arc of a circle, it can be given an orientation. We assign menisci an orientation such that the non-wetting phase is to the left. (For wetting angles in the range $[0, \pi/2)$ this implies the meniscus center of curvature is to the left.) Each oriented meniscus has a start and and end point. These points are in contact with perimeter components. We classify menisci by a two-part label consisting of "start point component type"-"end point component type". Thus there are edge-edge, edge-vertex, vertex-edge and vertex-vertex menisci.

Consider an arbitrary meniscus M_1. Beginning at the start point of M_1 and following M_1, a directed circuit is constructed as follows. The end point of M_1 will contact a perimeter component. The directed circuit continues onto the perimeter component in the counterclockwise direction. If a start point of another meniscus (e.g. M_2) is encountered, the directed circuit moves onto M_2. This circuit construction is continued: at the end-point of a meniscus, the circuit branches onto the perimeter in the counterclockwise direction; when the start point of a meniscus is encountered, the circuit branches onto the meniscus. Circuit construction terminates when the start point of a previously discovered meniscus, or the perimeter component where we initiate the construction is reached. We refer to the so-constructed circuit as a "counterclockwise circuit" (CC-circuit for short). There is an analogous "clockwise circuit" (C-circuit), where the circuit continues at any meniscus end point by branching onto the perimeter component in a clockwise direction.

Fig.3 illustrates a CC-circuit construction: $M_1, E_7, E_6, M_2, E_2, M_3, E_9$. The above definition of a CC-Circuit assumes that the arc-menisci are known. In the later sections we will describe the construction of a CC-circuit which includes tests of existence and subsequent construction of menisci as the circuit is being developed.

A necessary condition for a configuration of menisci to be physically consistent is: the interior (left side) of every CC-circuit contains only non-wetting fluid; the interior (left side) of every C-circuit contains only wetting fluid;

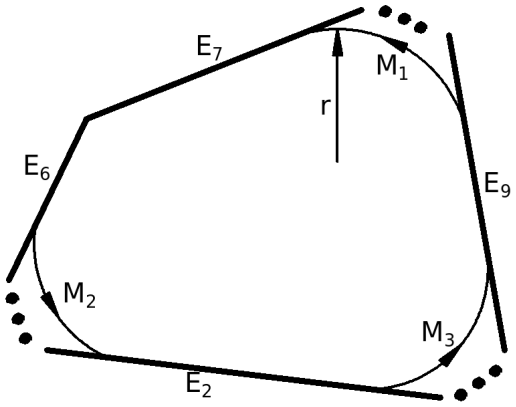

Figure 3: Illustration of a single counterclockwise-circuit contacting only edge components. There are 9 edges in the perimeter, only the four edges that form the CC-circuit are shown.

and the union of CC-circuit and C-circuit interiors forms the interior of the polygon. The construction of CC-circuits containing non-wetting fluid is the basis behind our construction algorithm. The algorithm is greedy in that it constructs a CC-circuit using local information. After constructing one CC-circuit it looks for opportunity to construct the next possible CC-circuit. The algorithm terminates when all possible menisci have been assigned to a CC-circuit.

2.4 CC-circuit construction for a single non-wetting region

Each point p on the MA of a polygon interior is the center of a circle which is tangent to the polygon boundary at more than one point, and for which any so-centered circle of smaller radius lies entirely inside the interior. The

radius of this tangential circle defines a distance function $d(p)$ on the MA. The radius function has the range $[0, R_{\text{mic}}]$ where R_{mic} corresponds to the radius of the maximally inscribed circle in the polygon. The MA for an polygon interior is a tree, with the property that a root p_r can be chosen such that $d(p_r) = R_{\text{mic}}$ and all leaf points p_l satisfy $d(p_l) = 0$. There is a similar distance function associated with every point on a drainage axis $DA(\theta)$. Consider a polygon with the following property for $DA(\theta)$: $d(p)$ monotonically increases from each leaf point to the root. Then such a polygon will develop a single, connected, non-wetting region during drainage [36].

We describe the construction of a CC-circuit which, for initial discussion, we assume contacts only edge components (i.e. the circuit contains only edge-edge menisci). Such a circuit was shown in Fig.3. The construction of the CC-circuit, for which all menisci have a pre-determined radius of curvature r, proceeds as follows. Fix an arbitrary edge, without loss of generality E_n, as the first "base" edge. The remaining edges, $\{E_1, \ldots, E_{n-1}\}$, form a list of "partner" edges. Moving clockwise through the partner edges, for each partner edge we determine whether there exists a meniscus of radius r whose start-point lies on the base edge and whose end point lies on the partner edge. If no meniscus can be located between the base edge and any partner edge in the list, the base edge is advanced counterclockwise (e.g. to E_{n-1}) and its partner list created. For base edge E_{n-1}, the partner list would be $\{E_n, E_1, \ldots, E_{n-2}\}$. The first time a meniscus is successfully located between a base edge and a partner edge, the remainder of the procedure is similar

Base component	Partner list	Meniscus added to CC-circuit
E_9	$E_1, E_2, \ldots, E_8$	M_1
E_7	$E_9, E_1, \ldots, E_6$	
E_6	$E_7, E_9, E_1, \ldots, E_5$	M_2
E_2	E_6, E_7, E_9, E_1	M_3

Table 3: The sequence to construct CC-circuit in Fig.3.

with this step but some slightly adjustment to continue the construction of a CC-circuit.

An entire CC-circuit construction is briefly described using Fig.3 as reference. The first base edge is E_9 having partner list $\{E_1, E_2, \ldots, E_8\}$. Meniscus M_1, having start point on E_9 and end point on E_7 is located. The base edge moves to E_7 having partner list $\{E_9, E_1, \ldots, E_6\}$. Note the partner list for E_7 does not include E_8 as this edge is excluded by the presence of meniscus M_1. No meniscus having start point on E_7 and end point on its partner list is located. The base edge moves to E_6 having partner list $\{E_7, E_9, E_1, \ldots, E_5\}$. Meniscus M_2, having start point on E_6 and end point on E_2 is located. The base edge moves to E_2 having partner list $\{E_6, E_7, E_9, E_1\}$. (Edges E_5, E_4, and E_3 are now precluded from the partner list by the presence of M_2.) Meniscus M_3, having start point on E_2 and end point on E_9 is located. As E_9 contains the start point of meniscus M_1, a CC-circuit has been computed and the circuit construction terminates. The whole process can be summarized into Table 3.

Instead of counterclockwise we check the partner list clockwise, although

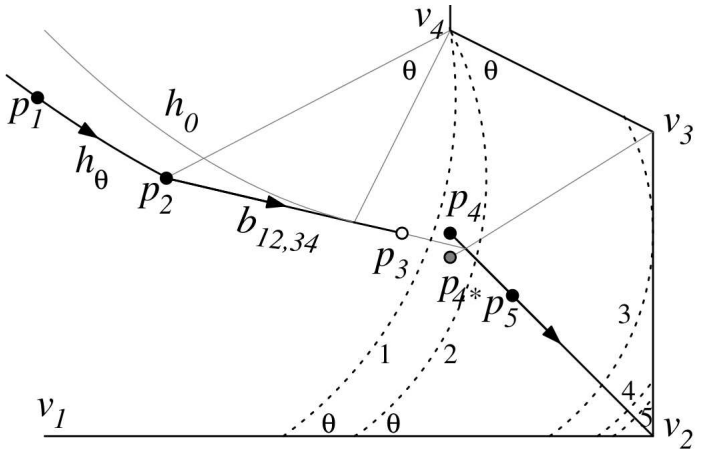

Figure 4: Illustration of a drainage axis (DA) [36]. Dark solid lines are DA when the wetting angle is greater than 0; light grey lines are medial axis(MA). Dot arcs are menisci.

it seems that counterclockwise is more efficient to discover the meniscus. For example, in Fig.3 when the base edge is E_9, we check the partner list clockwise seven times before M_1 is located. However, if we do it counterclockwise, only two partner checking, E_8 and E_7, are needed. Attractive it seems to be, we can't check the partner list in counterclockwise, as the simulation must follow the inner physics of drainage process. Fig.4 illustrates the drainage axis when the wetting angle is greater than 0. When the inlet pressure increases, the meniscus is pushed moving from position 1 to position 5 with a shrinking radius, and the trajectory of the menisci center forms dark solid curve. No matter what simulation method we adopt, the centers of the menisci must lie on the drainage axis, otherwise, the simulation result is not true for drainage process.

In Fig.4, Meniscus 3 is not stable when it touches the boundary V_2V_3,

the meniscus splits into Meniscus 4 and Meniscus 4*. Because the wetting angle is too large for vertex V_3 to hold a meniscus, Meniscus 4* doesn't exist and only Meniscus 4 is left. The corresponding center is P_4. If we assume the current radius of meniscus is $r_3 + \epsilon$, from Fig.4, the position of the corresponding meniscus should be on the left side of Meniscus 3. If we fix edge V_1V_2 as the base and check the partner list (the rest of edges) clockwise, the correct meniscus, held between the base V_1V_2 and the partner V_3V_4 , could be located and the center also lies on the left side of P_3. However, if we check the partner list counterclockwise, a false meniscus between V_1V_2 and V_2V_3 is located. It is on the left side of Meniscus 4 and its center is also on the left side of P_4, which is not on DA, thus this false meniscus is invalid. Therefore, only clockwise is the correct direction to check the partner list.

Note that considering base edges in a counterclockwise manner and listing partner edges in a clockwise manner ensure that the smallest area CC-circuit is created. This choice ensures that we do not create a CC-circuit that encloses two (or more) non-wetting regions and one (or more) wetting regions.

With the successful construction of the (by assumption) single CC-circuit comprising menisci with radius of curvature r, the parameters α_i, L_{NS} and A_N in (4) can be computed geometrically. Evaluation of the left-hand-side of (4) will give a result that is either positive, negative or zero. If zero, the entry-pressure meniscus configuration has been constructed and the entry pressure can be computed from the value of r using the Young-Laplace condition (3). If positive, the pre-determined radius r is too large and a CC-circuit must

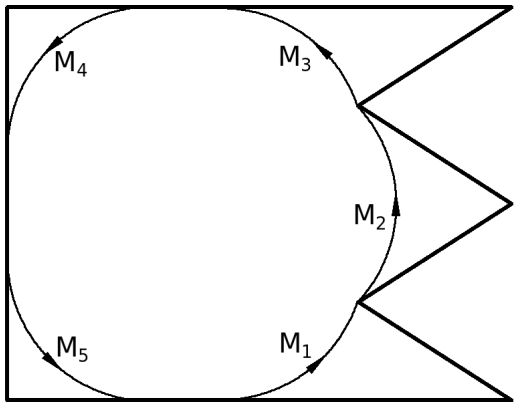

Figure 5: Four types of counterclockwise menisci. M_1 is an edge-vertex meniscus, M_2 is vertex-vertex, M_3 is vertex-edge, M_4 and M_5 are edge-edge.

be constructed with a smaller radius of curvature. If negative, a CC-circuit must be constructed with a larger radius of curvature.

Due to the existence of reflex vertices the nonlinear Eq.(4) as a function of r may contain some points which have sharp slopes. We therefore adopt Brent methods which combine the efficiency of inverse quadratic interpolation as well the robustness of the bisection method [5] to solve Eq.(4).

Having illustrated the core of the CC-circuit construction assuming that only edge-edge menisci are involved, we must now include meniscus types that include reflex vertices since pinning of menisci can occur on reflex vertices (concave "corners" of the polygon) but not on vertices corresponding to convex corners of the polygon. Fig. 5 illustrates the appearance of all four types of menisci in one CC-circuit. It is clear that the core decision making of a CC-circuit, branch counter-clockwise at the end-point of a meniscus, branch onto a meniscus at its start point, remains unchanged.

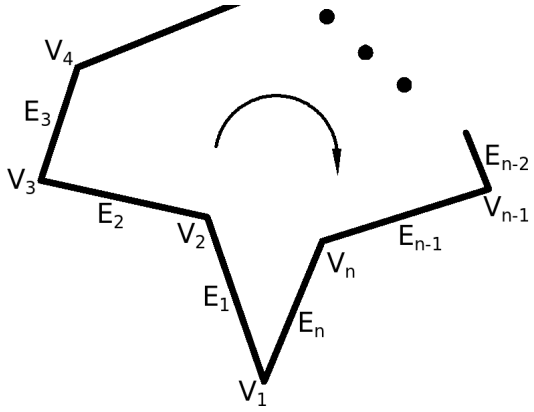

(a)

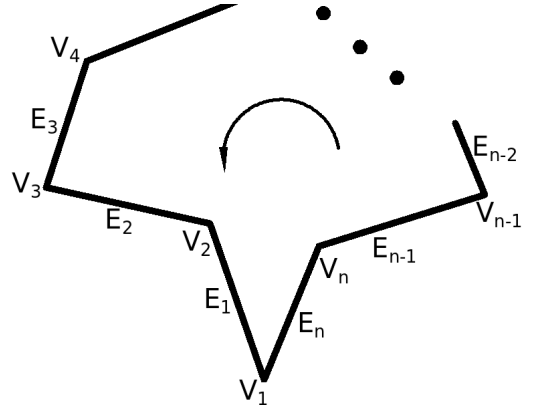

(b)

Figure 6: (a) partner component lists are filled in a clockwise direction. (b) base components are switched in a counterclockwise direction.

We refer to Fig.6 to clarify inclusion of reflex vertices into base- and partner-component lists. The initial boundary list for this perimeter is $\{E_1, V_2, E_2, E_3, E_4 \ldots V_n, E_n\}$. Assuming E_1 is arbitrarily chosen as the first base component to be considered, its partner list is $\{V_2, E_2, E_3 \ldots V_n, E_n\}$. Note the partner list consists of edge and reflex vertices ordered in a clockwise direction (as indicated in Fig.6a). Tests (described in later sections) are performed to determine whether a physical meniscus of pre-determined radius r exists between this base component and each successively ordered partner component. And the results of the tests have two possibilities:

1. If no such meniscus is located, the base component is changed, proceeding in a counterclockwise direction as indicated in Fig.6b, to E_n and its partner list $\{E_1, V_2, E_2, E_3 \ldots V_n\}$ created;

2. Otherwise, a physical meniscus was located, for instance between base edge E_1 and the reflex vertex V_n, then this meniscus becomes the first element in the CC-circuit, and the base component is moved to V_n. The partner list for V_n will be $\{E_n, E_1, V_2, E_2 \ldots E_{n-1}\}$.

Construction of the CC-circuit proceeds by iterating this procedure as described in Fig.3 where only edge components are involved. This method includes two loops producing an algorithmic complexity of $O(n^2)$. The inner loop sweeps clockwise through the partner component list, testing for the first occurrence of a physical meniscus with the given base component. The outer loop sweeps the boundary list (amended by the portion of the CC-circuit constructed "to date") in a counterclockwise direction to complete a

physical CC-circuit. Both loops leverage the idea of a "greedy" method, by making local choices to determine the smallest possible physical CC-circuit: the inner loop stops when the first physical meniscus is found; the outer loop follows the CC-circuit built "to date" to switch to the next base component.

What remains to be described are the base-component, partner-component tests mentioned above that are needed to determine the next physical meniscus to include in the CC-circuit.

2.5 Base-component, partner-component meniscus tests

In the construction of a CC-circuit, for each base-component and partner-component pair, a test must be performed to determine whether a meniscus, of radius-of-curvature r, exists between the two components. The base component must be the site of the start point of the meniscus, the partner component the site of its end point. We describe the four types of tests encountered.

2.5.1 Edge-edge meniscus

In Fig.7, AB denotes the base edge; DE the partner edge. F denotes the point of intersection of the straight lines defined by these two edges; β denotes the angle subtended by these two lines at F. For drainage we have the restriction $\theta + \beta/2 \leq \pi/2$ [36]. For a meniscus of radius r to have start-point on AB and end-point on DE, the coordinates of the center of curvature C

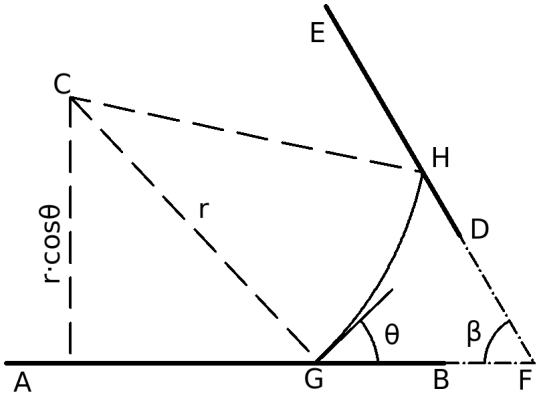

Figure 7: The geometry for an edge-edge arc.

of the arc are given by the linear system

$$\begin{cases} (\overrightarrow{CA} \times \overrightarrow{CB}) \cdot \overrightarrow{n} = r\cos\theta \cdot |\overrightarrow{AB}| \\ (\overrightarrow{CD} \times \overrightarrow{CE}) \cdot \overrightarrow{n} = r\cos\theta \cdot |\overrightarrow{DE}| \end{cases} \tag{5}$$

The start point G could be parametrized as $\overrightarrow{G} = \overrightarrow{A} + t_G\overrightarrow{AB}$, then we can locate G by solving t_G from the length of $\overrightarrow{FG}$:

$$|\overrightarrow{F} - \overrightarrow{A} - t_G\overrightarrow{AB}| = r \cdot \frac{\cos(\theta + \beta/2)}{\sin(\beta/2)} \tag{6}$$

The end-point H of the meniscus is determined by the length FH which satisfies $|FH| = |GF|$ by symmetry , and decided by the parametric t_H.

The start point G must lie on the base edge; the end point H on the partner edge. Thus the test which determines whether the arc constructed by Eq.(5) and Eq.(6) is a physical meniscus is that the parameter t_G and

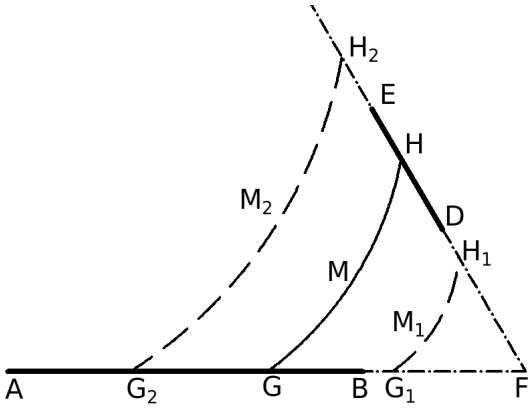

Figure 8: The test for an edge-edge arc. The arc M has start- and end-points in contact with the edge components – producing a physical meniscus; M_1 and M_2 do not.

t_H satisfy $t_G,\ t_H \in [0,1]$. If either condition fails, the arc does not contact both edge components, and no physical meniscus of radius r exists between the two edge components. Fig.8 illustrates the test. If the solution to Eq.(6) for G and the equivalent for H fall at positions G_1, H_1 or G_2, H_2, then the corresponding arc M_1 and M_2 do not contact both edges and are not physical. If the solutions fall at positions G, H, then the corresponding arc M is a physical meniscus.

For the special case that edges AB and DE are parallel, we prove (see Appendix) that no corresponding edge-edge can exist in a CC-circuit corresponding to an entry pressure configuration for a wetting angle in $[0, \pi/2)$.

2.5.2 Edge-vertex meniscus

Different from the test for an edge-edge meniscus, the test for an edge-vertex meniscus is not so intuitive. The reason is simple: the calculation of the edge-

vertex meniscus should not only match with geometry, but also the drainage process. Although Fig.4 has already illustrated the center trajectory of a meniscus in drainage process, to understand more details about the drainage process we need to review the process from another point of view.

In Fig.9, AB denotes the base edge; E the partner reflex vertex. Dash lines, named as "touching lines", are tangential with the menisci on the endpoint. With increasing of inlet pressure, the meniscus moves along edge AB with a shrinking radius, touching edge EF from position 0 initially, then pinning on vertex E at position 1, later unpinning on vertex E at position 2, and finally arriving at position 3. Meniscus M_1 is the last edge-edge meniscus between AB and EF, as the angle between the touching line T_1 and the extension of EF is still θ. If the inlet pressure keeps increasing, or the radius of meniscus keeps decreasing, the angle between the touching line and the extension of EF is less than θ, then the meniscus pins on vertex E, an edge-vertex meniscus comes into being. If inlet pressure continues to increase, the meniscus is pushed to position 2 where the angle between the touching line and DE regains to θ, thus an edge-edge meniscus between AB and DE appears. Note that only in the angle range between T_1 and T_2 can an edge-vertex meniscus exist. For simplicity we denote this angle as the "pinning angle" of vertex E.

Fig.10 gives two examples that edge-vertex arcs fall beyond the "pinning angle". Subplot (a) shows a meniscus M held between AB and EF. If M is moved to M', then M' could also "pin" on the vertex E which means

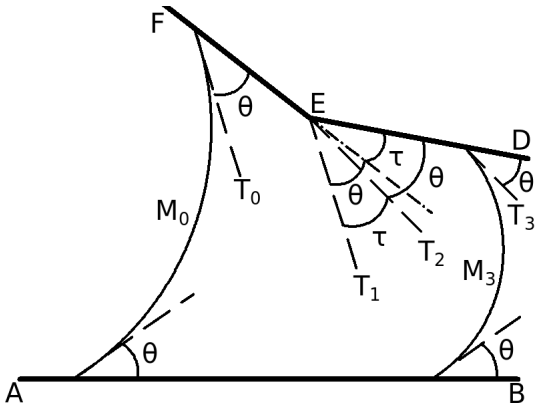

Figure 9: The drainage process near a reflux vertex. Dash dot line is the extension of edge EF, dash lines mark the tangential touching lines of the menisci and Arabic numerals represent different menisci positions. θ is the wetting angle. For simplicity M_1 and M_2 are omitted. In the whole process all of the menisci keep the same wetting angle θ with the base AB.

EF yields two menisci with AB for a given radius r. [36] indicates that the drainage radius should be monotonic, so the two menisci are conflicting. Between the two conflicting menisci M and M', we can easily justify that only M is valid because δ, the angle between the touching line of M' and the extension of EF, is greater than θ, which clearly reveals the arc M' is not in the "pinning angle" of E shown in Fig.9. In fact, the touching line of M' lies on the left side of T_1 in Fig.9, and that region belongs to the touching line of edge-edge meniscus between AB and EF, thus M' is not realistic in drainage.

The similar situation happens on Fig.10(b) where the correct meniscus M should touch edge DE without "pinning" on the vertex E. As the meniscus on the position of M regains the wetting angle θ with the edge DE, the meniscus should have already "unpinned" with vertex E. Again, the corresponding position of touching line of M' in Fig.9 is in the right side of T_2, as

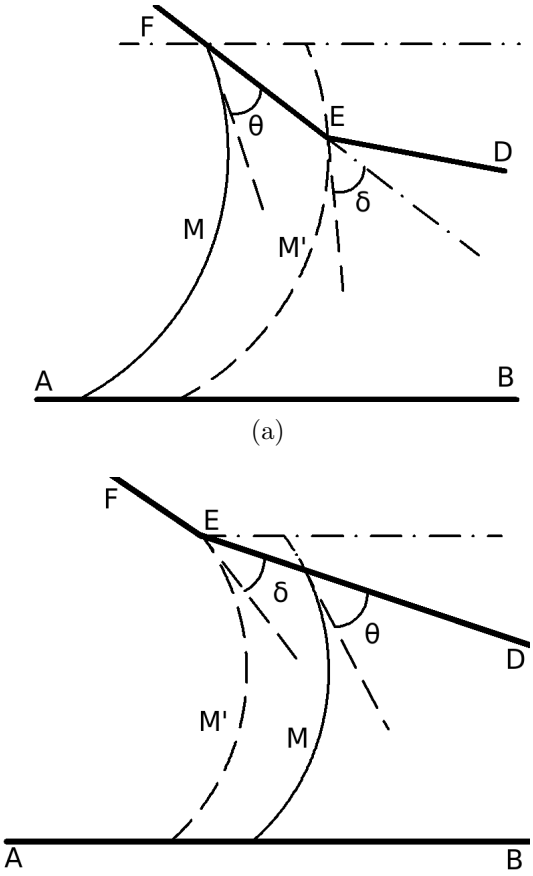

Figure 10: Two cases lead to false edge-vertex menisci. All arcs have the same radii.

a result M' is also false.

Fig.10 discloses the fact that the edge-vertex meniscus is only a subset of the edge-vertex arc, so it is necessary to test if an edge-vertex arc can pin on the reflex vertex. To do this we must ensure that no possible physical solution, having radius r, exists between the base-edge and partner-edge pairs AB, DE or AB, EF as illustrated in Fig.11.

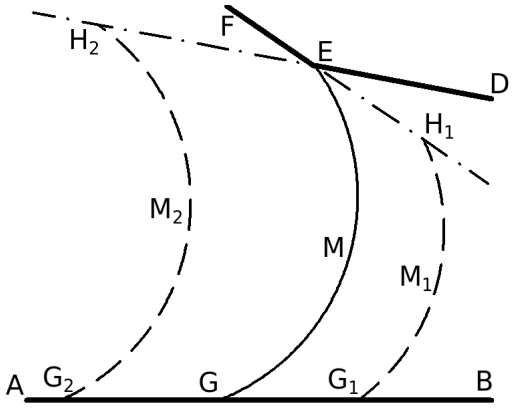

Figure 11: The test for an edge-vertex arc. The arc M has start- and end-points in contact with the perimeter components – producing a physical meniscus; arcs M_1 and M_2 do not. All the three arcs have the same radius of curvature.

To implement these tests we compute the possible position pairs H_1 and H_2 from Eq.(6). For a meniscus to pin on reflex vertex E, we must also determine that $t_{H_1} < 0$ and $t_{H_2} > 1$, as illustrated in Fig.11 (arcs M_1 and M_2).

Only if the above conditions are satisfied, a meniscus can pin on the reflux vertex. Fig.12 illustrates how to locate the edge-vertex meniscus. The coordinates of the center point for an arc of radius r between the two components are given by solving the quadratic system

$$\begin{cases} (\overrightarrow{CA} \times \overrightarrow{CB}) \cdot \overrightarrow{n} = r \cos\theta \cdot |\overrightarrow{AB}| \\ |\overrightarrow{CE}|^2 = r^2 \end{cases} \tag{7}$$

If the quadratic equation has no solution, the pre-determined radius r is too

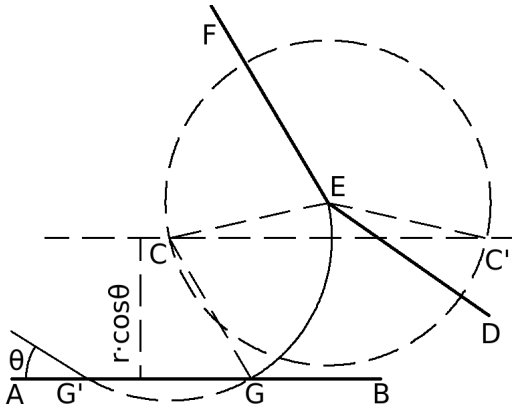

Figure 12: The geometry for an edge-vertex arc.

small; and an arc in contact with vertex E never touches the straight line defined by AB. If the equation has two solutions, as illustrated in Fig.12 (points C and C') only one solution, C, is correct. (An arc centered in C' will contact AB at wetting angle $\pi - \theta$, not θ as required.) The intersection G of the arc with the straight line defined by AB is given by parameter t_G from solving of

$$|\overrightarrow{C} - \overrightarrow{A} - t_G\overrightarrow{AB}| = r^2, \tag{8}$$

A physical solution to Eq.(8) requires $t_G \in [0, 1]$. The solution to the quadratic system may produce two values t_G and $t_{G'}$ both of which satisfy $t_G, t_{G'} \in [0, 1]$ as illustrated in Fig. 12. The solution with the larger positive t-value is the correct one. (In Fig. 12, the point G corresponds to the correct solution.)

In sum, with tests on $t_G \in [0, 1]$, $t_{H_1} < 0$ and $t_{H_2} > 1$ appropriately

satisfied, a physical edge-vertex meniscus pinning on reflex vertex E exists.

In a special case arc M_1 or M_2 may not exist at all which is shown in Fig.13. For a meniscus to exist between any two edges, it must satisfy $\theta + \beta/2 \leq \pi/2$, where β is the angle (towards the interior of the polygon) between the two edges. Thus if the angle β, spanning from $\overrightarrow{BA}$ to $\overrightarrow{EF}$ clockwise (as indicated in subplot (a)) exceeds $\pi - 2\theta$, arc M_1 can never exist and the test for t_{H_1} need not to be performed. Similarly, if the angle spanning clockwise from $\overrightarrow{BA}$ to $\overrightarrow{DE}$ is beyond this restriction in subplot (b), M_2 doesn't exist either.

2.5.3 Vertex-edge meniscus

Determining whether a physical, pinned meniscus of radius r exists between the base vertex and partner edge requires analogous computation to what described for the edge-vertex case, we also need to perform two additional edge-edge meniscus tests which calculate the location of two possible arcs in Fig.14, where E denotes the base reflex vertex; AB the partner edge. If the parameter pairs H_1 and H_2 derived from Eq.(6) make the conditions $t_{H_1} < 0$ and $t_{H_2} > 1$ hold for the given r, we continue to locate the vertex-edge meniscus.

We use the same equations with Eq.(7)to locate the center of the arc shown in Fig.15.

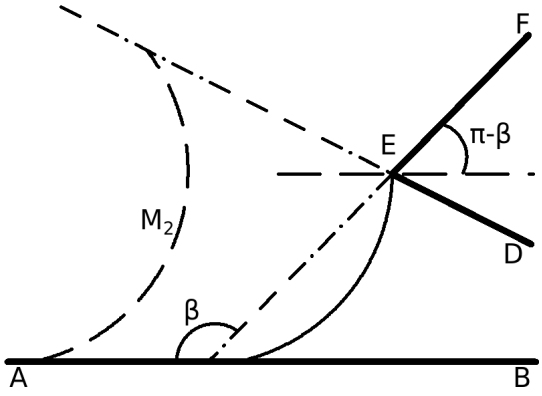

(a)

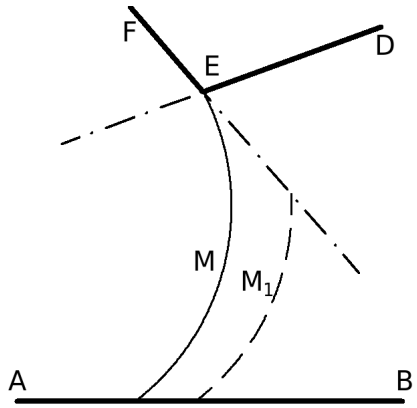

(b)

Figure 13: Special cases for the edge-vertex tests. All arcs have the same radius of curvature.

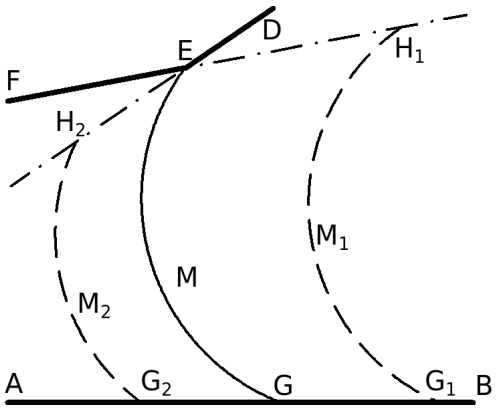

Figure 14: The test for a vertex-edge arc. The arc M has start- and end-points in contact with the perimeter components – producing a physical meniscus; arcs M_1 and M_2 do not. All the three arcs have the same radius of curvature.

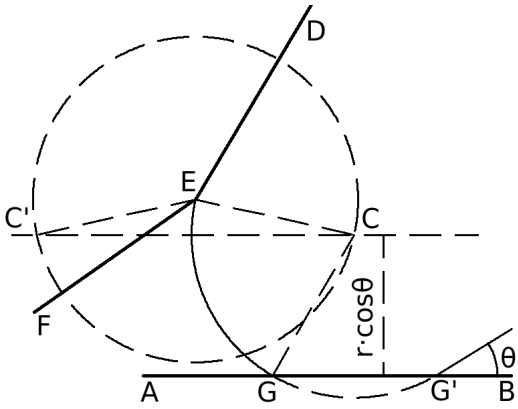

Figure 15: The geometry for a vertex-edge arc.

$$\begin{cases} (\overrightarrow{CA} \times \overrightarrow{CB}) \cdot \overrightarrow{n} = r\cos\theta \cdot |\overrightarrow{AB}| \\ |\overrightarrow{CE}|^2 = r^2 \end{cases} \tag{9}$$

However, this time the right side of the two solutions, C, is correct, and the left side solution C' yields a false arc with wetting angle $\pi - \theta$. The other endpoint G of the arc intersecting with AB is given by parameter t_G from solving of

$$|\overrightarrow{C} - \overrightarrow{A} - t_G\overrightarrow{AB}| = r^2, \tag{10}$$

And in the two solutions only the left one, G with smaller t-value in $[0, 1]$, is correct.

In sum, the three required tests on $t_G \in [0, 1]$, $t_{H_1} < 0$ and $t_{H_2} > 1$ determine that a physical vertex-edge meniscus pinned on reflex vertex E exists.

Also similar with the edge-vertex case, in a special case shown in Fig.16 arc M_1 or M_2 may not exist at all. In subplot (a) we only need to calculate M_1 and test $t_{H_1} < 0$ if the angle spanning from $\overrightarrow{AB}$ to $\overrightarrow{ED}$ counterclockwise (as indicated in subplot (a)) exceeds $\pi - 2\theta$; in subplot (b) the missing M_1 leads to the only test $t_{H_2} > 1$ is required.

2.5.4 Vertex-vertex meniscus

Similarly with analysis of edge-vertex meniscus and vertex-edge meniscus, to ensure that a physical vertex-vertex meniscus pinning on both reflex vertices

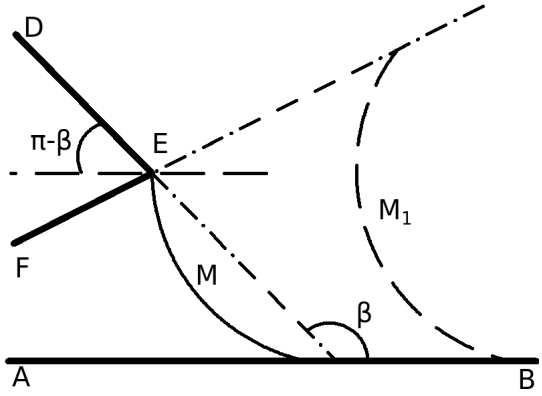

(a)

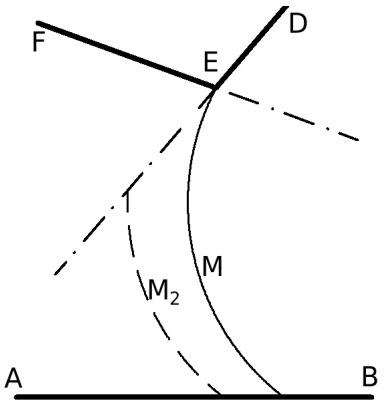

(b)

Figure 16: Special cases for vertex-edge tests. All arcs have the same radius of curvature.

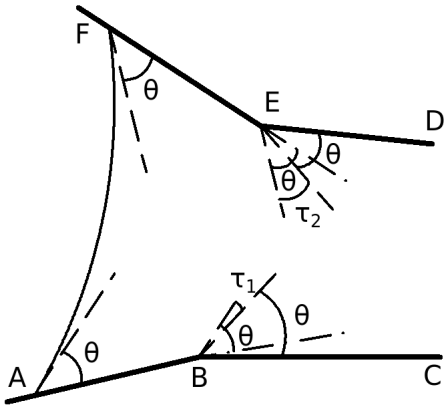

Figure 17: The drainage process near two reflux vertices. Dash dot line is the extension of edge AB and EF, dash lines mark the tangential touching lines of the menisci on the endpoints. θ is the wetting angle .

exists, we must ensure that the meniscus falls onto the "pinning angle" of the two reflux vertices at the same time. Fig. 17 illustrates the "pinning angle", τ_1, of the base reflux vertex B and τ_2 of the partner vertex E. The corresponding vertex-vertex meniscus must fall onto τ_1 and τ_2 simultaneously.

To justify if a meniscus can pin on the two reflux vertices, we adopt the two vertex-edge tests indicated in Fig.18a and the two edge-vertex tests indicated in Fig.18b. As seen in Fig.18a, the computations for M_1 and M_2 by Eq.(9) and Eq.(10) must yield $t_{H_1} < 0$ and $t_{H_2} > 1$. Similarly in Fig.18b, the computations for M_3 and M_4 by Eq.(7) and Eq.(8) must return $t_{H_3} > 1$ and $t_{H_4} < 0$.

If the above four conditions hold, we resume to locate the position of the vertex-vertex meniscus. In Fig.19, B denotes the base reflex vertex; F the partner reflex vertex. The coordinates of the center point for an arc of radius

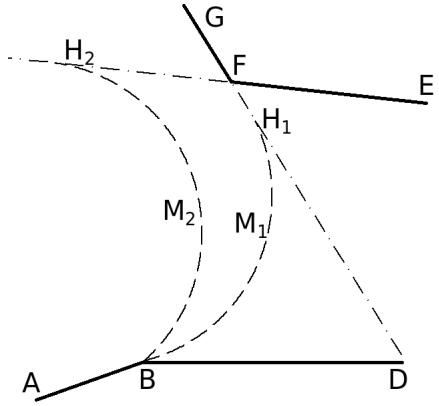

(a)

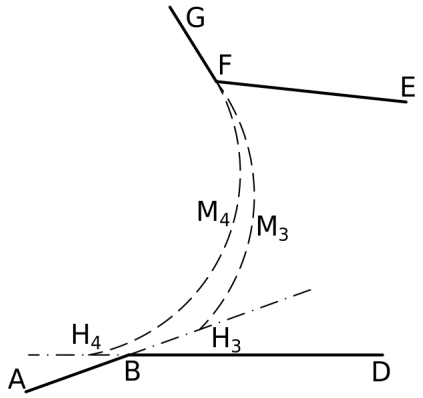

(b)

Figure 18: Illustration of the vertex-edge tests (a) and edge-vertex tests (b) required to indicate that a physical vertex pinning on both reflex points B and F exists.

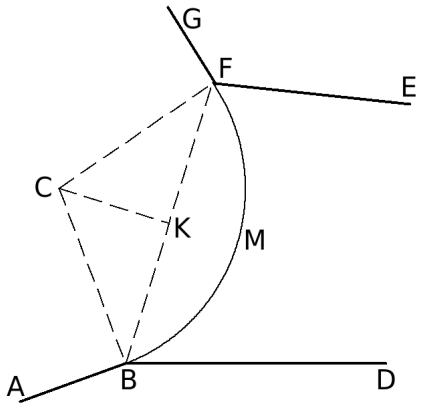

Figure 19: The geometry for a vertex-vertex arc.

r between the two components are given by solving the linear system

$$\begin{cases} \overrightarrow{CK} \cdot \overrightarrow{BF} = 0, \\ (\overrightarrow{CB} \times \overrightarrow{CF}) \cdot \overrightarrow{n} = |\overrightarrow{BF}| \cdot |\overrightarrow{CK}| = |\overrightarrow{BF}| \cdot \sqrt{r^2 - \dfrac{|\overrightarrow{BF}|^2}{4}}, \end{cases} \tag{11}$$

where K is the middle point of the segment BF. As r and $|\overrightarrow{BF}|$ is known, the linear equations yield only one unique solution C.

In sum, only if the tests of $t_{H_1} < 0$, $t_{H_2} > 1$, $t_{H_3} > 1$ and $t_{H_4} < 0$ hold, a vertex-vertex meniscus pinning on the two reflux vertices exists.

Depending on the position of the two reflux vertices, the vertex-edge arcs M_1 and M_2 in Fig.18a, likewise the edge-vertex arcs M_3 and M_4 in Fig.18b may not exist. Fig.20 gives four individual examples. To form an edge-vertex meniscus, Fig.12 specifies that the partner reflux vertex E must lie on the left side of the base $\overrightarrow{AB}$, as well a vertex-edge meniscus in Fig.15 also requires the base reflux vertex E is on the left side of the partner $\overrightarrow{AB}$. However, M_1,

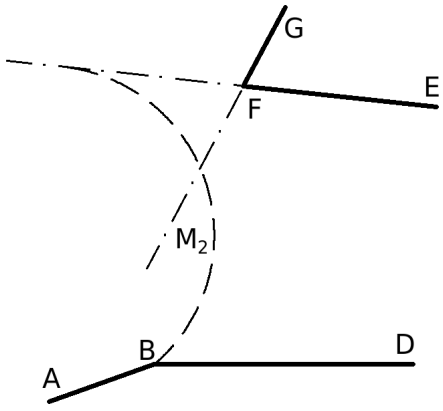

(a)

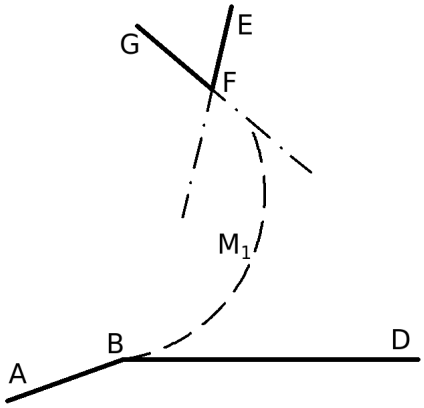

(b)

Figure 20: Special cases for vertex-vertex meniscus tests.

M_2, M_3 and M_4 may not satisfy this requirement, thus they may not be valid even in geometry. In those cases we only need to check if the rest of menisci satisfy the test conditions.

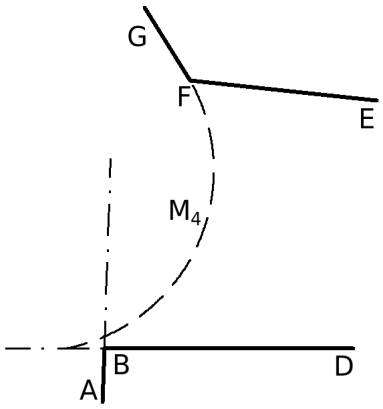

(c)

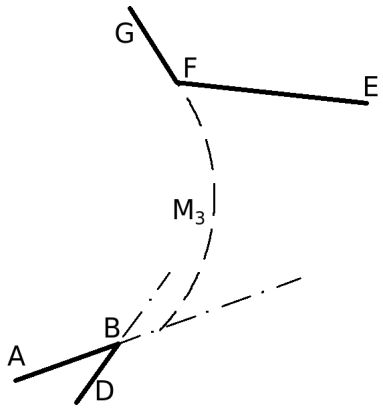

(d)

Figure 20: Special cases for vertex-vertex meniscus tests.

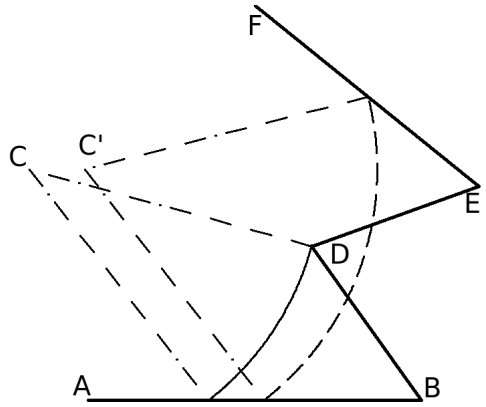

Figure 21: Collision of a prospective edge-edge meniscus with other boundary edges. AB is the base-edge and EF is the partner-edge.

2.6 Meniscus validation

The existence of a physical meniscus cannot always be solely determined by the local base-component, partner-component tests described above. Fig.21 illustrates a test for an edge-edge meniscus between base edge AB and the current partner edge EF. Although the test succeeds, this meniscus is still invalid, as it intersects with boundary BD and DE. Thus the process of partner checking continues in clockwise until the correct partner component - vertex D is found. The final valid meniscus is an edge-vertex meniscus, not an edge-edge meniscus.

2.7 Uniqueness of CC-circuits

Construction of a CC-circuit should not depend on the choice of the first base component. Fig.22 illustrates that how this is achieved. The figure shows a CC-circuit consisting of menisci M_2, M_3 and M_4. The boundary

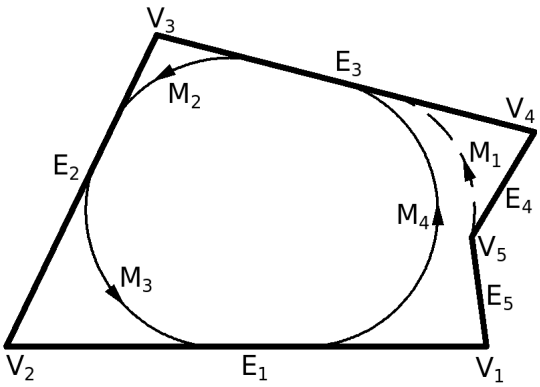

Figure 22: Illustration for automatic culling of extraneous meniscus that may be generated during CC-circuit construction.

component list (of edges and reflex vertices) consists of $E_1, E_2, E_3, E_4, V_5, E_5$. If any of the edges is chosen as the first base component, the constructed CC-circuit should only contain these three menisci (and corresponding edges). However, if the vertex V_5 is chosen as the first base component the CC-circuit construction starts with the meniscus sequence M_1, then M_2 and M_3. After finding M_3, the base edge moves to E_1. The first physical meniscus located on E_1 is the edge-edge meniscus M_4. Inclusion of M_4 in the CC-circuit completes a circuit without meniscus M_1. M_1 is therefore excluded from the CC-circuit construction. As a result, the computed non-wetting region (CC-circuit interior) is independent of starting base component.

The appearance of "extraneous" menisci such as M_1 above results from the local nature of the algorithm. However, as we see from the above example, these extraneous menisci are naturally excluded by the end of a CC-circuit construction.

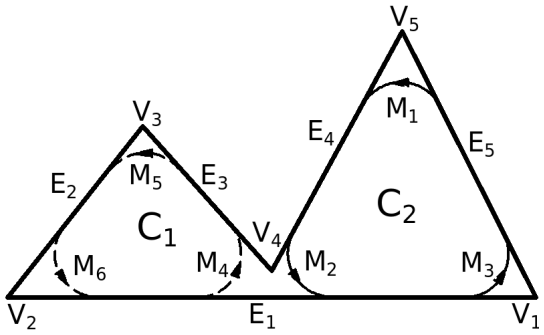

Figure 23: A throat cross section supporting two CC-circuits (two non-wetting regions) corresponding to different radius solutions to (4).

2.8 Multiple non-wetting regions

Fig.23 shows a "comb"-like polygon which supports two possible non-wetting regions C_1 and C_2, each of them satisfies Eq.(4) with different entry radii r_{e1} and r_{e2}. The region with the larger entry radius, corresponding to small capillary pressure will be the correct initial entry condition for drainage. However, under increasing capillary pressure, subsequent non-wetting phase entry into the second region will occur. In order to determine both CC-circuits (and determine which corresponds to the lower pressure initial entry condition), our algorithm must pay attention to boundary segments that are "excluded" in the construction of a CC-circuit.

We use Fig.23 to illustrate the procedure. Assume the CC-circuit construction begins with edge E_5 as base component. The CC-circuit construction is detailed in the Table 4 corresponding to the starting base-component of E_5. The whole construction is based on a fixed radius r, and by Brent

Start base	Base component	Partner list	Meniscus added to CC-circuit
E_5	E_5	E_1, E_2, E_3, V_4, E_4	M_1
	E_4	E_5, E_1, E_2, E_3, V_4	M_2
	E_1	E_4, E_5	M_3
V_4	V_4	E_4, E_5, E_1, E_2, E_3	
	E_3	V_4, E_4, E_5, E_1, E_2	M_5
	E_2	E_3, V_4, E_4, E_5, E_1	M_6
	E_1	E_2, E_3, V_4, E_4	M_4

Table 4: The sequence to search different non-wetting regions.

Method [5] we can locate the CC-circuit with entry radius corresponding to the non-wetting region C_2.

Note in particular, once meniscus M_2 is added to the CC-circuit, its presence removes perimeter components E_2, E_3 and V_4 from the partner list constructed for base component E_1, otherwise E_1 will mislead to M_4 which is not in CC-circuit C_2. In the construction of CC-circuit C_2, inclusion of meniscus M_2 separated the perimeter components E_2, E_3 and V_4 from the rest E_1, E_4, E_5 of the perimeter. We therefore need to consider to investigate the separated component list E_2, E_3 and V_4 for other possible CC-circuits.

Assume we check the separated components in counterclockwise, then V_4 is the starting base component now. The edge-edge meniscus M_2 implies a successful edge-edge test prevents a low priority vertex-edge meniscus from come into being, so there is no meniscus exists from V_4 to its candidates. Then from next base component E_3, another CC-circuit C_1 containing menisci M_4, M_5 and M_6 is then located.

In the process of searching different CC-circuits, the key part is trimming unnecessary candidate partner components can guarantee that when the base component searches the proper partner, the checking always focuses on the components in the current CC-circuit. Thus no matter where the algorithm starts, all of the possible CC-circuits could be found. The logic described here is implemented by tagging perimeter components as having been "visited" during a CC-circuit construction. Use of tagging results in a search algorithm for all CC-circuits that has complexity $O(n^2)$.

2.9 Complexity improvement

The $O(n^2)$ greedy method discussed above is complete to construct CC-circuits and find the entry radius, however, our efforts to implement a fast method don't stop here. During the construction of CC-circuit a lot of trigonometry functions are employed to locate menisci and test their validation, nevertheless, trigonometry functions are more expensive for CPU than the basic algebra calculations. To promote the calculation efficiency, we should try to avoid the slow trigonometry functions as much as we can.

The scheme to speed up the calculation is to design a preprocessor which only picks up perspective partners to further process with expensive trigonometry functions. Fig.24 and Fig.25 illustrate the scheme, we assume all of the partners are edges. The processor is designed basing on the two observations.

a) Fig.7 shows only a partner with the lower right endpoint could hold a meniscus with the base AB under the wetting angle θ in $[0, \pi/2)$. The right

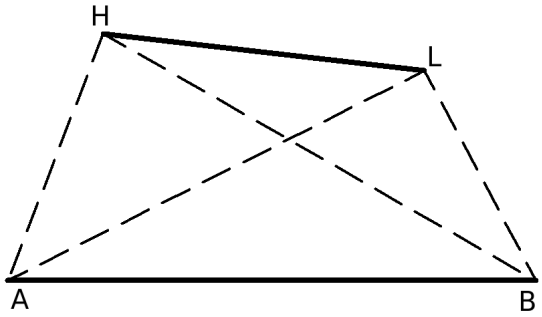

Figure 24: Scheme A to pick up a proper partner. Edge AB is the base. The right endpoint L should be lower than the left endpoint H.

endpoint of the partner is denoted as L, and left endpoint as H. Fig.24 also shows such a partner LH should satisfies the criteria:

$$|\overrightarrow{HA} \times \overrightarrow{HB}| > |\overrightarrow{LA} \times \overrightarrow{LB}| \tag{12}$$

b) For a wetting angle θ, the final meniscus, if it is held by the base AB, must lie on the region $ABFG$ which spans between two arcs whose chord length are $2r \cdot \cos\theta$ shown in Fig.25. Thus if a partner doesn't touch this region, it is impossible to form a meniscus with the base AB. While this region consists of two edges and two arcs, and it is complicated to test the intersection of a partner edge and this irregular region, we can extend the region $ABFG$ to a rectangle $ADEG$. The boundary point G is decided by:

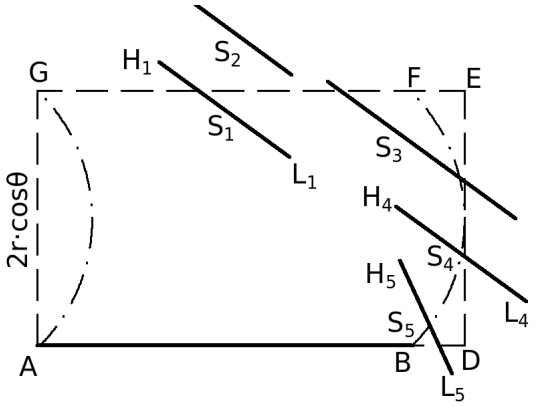

Figure 25: The scheme to pick up the proper partners. Dash lines mark a region where the perspective meniscus exists. Edge AB is the base. The other edges are the possible partners.

$$\begin{cases} (\overrightarrow{GA} \times \overrightarrow{GB}) \cdot \overrightarrow{n} = 2r\cos\theta \cdot |\overrightarrow{AB}|, \\ \overrightarrow{GA} \cdot \overrightarrow{AB} = 0, \end{cases} \tag{13}$$

And point D is located by solving parameter t_D from:

$$|\overrightarrow{A} + t_D \cdot \overrightarrow{AB} - \overrightarrow{B}| = r - r\sin\theta, \tag{14}$$

If point D is known, then point E is:

$$\begin{cases} (\overrightarrow{EA} \times \overrightarrow{EB}) \cdot \overrightarrow{n} = 2r\cos\theta \cdot |\overrightarrow{AB}|, \\ \overrightarrow{DE} \cdot \overrightarrow{AB} = 0, \end{cases} \tag{15}$$

After the points D, E and G are located, the rectangle $ADEG$ is fixed. The next step is to test if a partner edge touches this rectangle region. If so, then this partner is treated as a perspective partner; otherwise it is discarded.

There are two types of partners which can touch the rectangle region $ADEG$ according to the position of a partner's right endpoint L.

1) The first case is point L falls onto the rectangle region $ADEG$, which means L should be on the left side of AD, DE, EG and GA if L is not on the rectangle boundary. Then L should satisfies four left tests [45]:

$$\begin{cases} (\overrightarrow{LA} \times \overrightarrow{LD}) \cdot \overrightarrow{n} \geq 0 \\ (\overrightarrow{LD} \times \overrightarrow{LE}) \cdot \overrightarrow{n} \geq 0 \\ (\overrightarrow{LE} \times \overrightarrow{LG}) \cdot \overrightarrow{n} \geq 0 \\ (\overrightarrow{LG} \times \overrightarrow{LA}) \cdot \overrightarrow{n} \geq 0 \end{cases} \tag{16}$$

Fig.25 shows the right endpoint L_1 of the partner S_1 is in the region $ADEG$ and the partner S_2 is not.

2) The other case is that point L is not in the region $ADEG$, but it intersects with the boundary BD or DE. The partner can't intersect with the base AB, as the polygon boundary is not twisted. Moreover, it is not necessary to test if a partner intersects with EG or GA, as this condition is redundant. A partner can't intersect with EG or GA without crossing BD or DE, provided that point L is not in the region $ADEG$ and point L is lower than point H. In Fig.25 S_3 illustrates the redundancy.

If S_5 intersects with BD, then the following holds [45]:

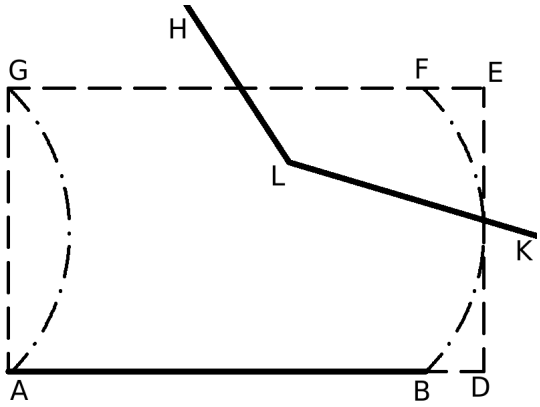

Figure 26: The scheme to pick up the proper reflux partner.

$$\begin{cases} (\overrightarrow{L_5B} \times \overrightarrow{L_5D}) \cdot (\overrightarrow{H_5B} \times \overrightarrow{H_5D}) \leq 0, \\ (\overrightarrow{BL_5} \times \overrightarrow{BH_5}) \cdot (\overrightarrow{DL_5} \times \overrightarrow{DH_5}) \leq 0. \end{cases} \tag{17}$$

Similarly, if S_4 intersects with DE, it should satisfy:

$$\begin{cases} (\overrightarrow{L_4D} \times \overrightarrow{L_4E}) \cdot (\overrightarrow{H_4D} \times \overrightarrow{H_4E}) \leq 0, \\ (\overrightarrow{DL_4} \times \overrightarrow{DH_4}) \cdot (\overrightarrow{EL_4} \times \overrightarrow{EH_4}) \leq 0, \end{cases} \tag{18}$$

Furthermore, this preprocessor is not only limited for an edge partner, it also works for a reflux vertex partner. Suppose this reflux vertex is L shown in Fig.26, in this case we only need to use Eq.(16) to check if the reflux vertex falls onto the rectangle region $ADEG$. This simple test can justify if Eq.(7) has solutions without solving a quadratic system.

The same idea could also be applied in the case of vertex-edge shown in Fig.27. The base vertex L should be in the rectangle region $ADEG$.

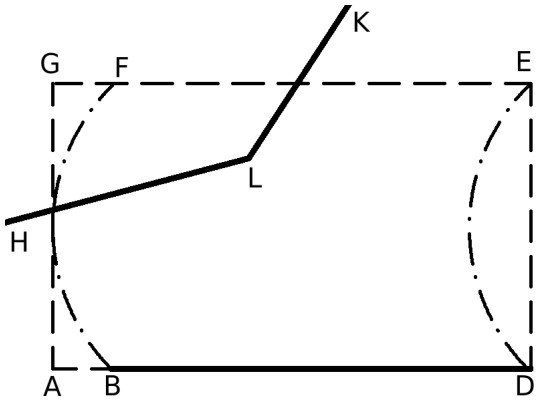

Figure 27: The scheme to pick up the proper edge partner.

In sum, we design a preprocessor to distinguish if a partner could hold a potential meniscus with the base before we employ the expensive trigonometry functions to locate the meniscus. Leveraging the preprocessor, the greedy method could reduce its complexity from $O(n^2)$ to $O(n)$ when the radius of curvature r is small, in other words, when the rectangle region $ADEG$ is not large. And a method with complexity in $O(n)$ is very efficient to deal with the large sample size of the cross sections.

θ	Failure amount	Failure rate
0°	131	0.0055
10°	78	0.0033
20°	30	0.0012
30°	17	0.0007
40°	10	0.0005

Table 5: Failure rate of the greedy algorithm.

3 Results

We have computed the entry radius for the sample of 23,639 throat polygons derived from the 3D analysis of tomography images of a Fontainebleau sandstone sample having 22% porosity. The computational failure rate is shown in Table 5. The calculation failure is defined as at least two menisci cross with each other, which contradicts the definition of a physically consistent CC-circuit. The number of failures decreases with the wetting angle increases, which is understandable as the number of menisci decline with the increasing of the wetting angle.

3.1 Drainage axis and entry menisci

While our primary goal is determination of an approximate predictor for values of the entry radius r_e, the CC-circuit construction can explore menisci configurations for any radius value (whether realized or not in drainage). For an arbitrary polygon, Fig.28 shows the trajectory of the centers of arc-menisci for a large range of radii of curvature. The trajectories are shown for four different wetting angles. For $\theta = 0°$ the trace of arc-menisci centers

should be identical to the medial axis (MA) of the polygon interior. This is verified in Fig.28(a). Also the trace of arc-menisci centers should construct the drainage axis for that wetting angle [36]. In Fig.28(c) and (d) we can observe some branches of MA are missing, as well some are disjointed and deformed. All of the observations match with the analysis of the drainage process in Fig.4. In fact, Fig.28 is the discretization of the drainage axis (DA) of a cross section.

Moreover, our results agree with Fig.2 well when we calculate the entry menisci using the Brent method[5] under the wetting angle $\theta = 0°$. The cross sections in Fig.2 are all throats which are able to hold only one single non-wetting region. Relatively simple as they are, they represent the majority of throat shapes in Fontainebleau sandstone sample.

Fig.29 shows the entry menisci of a more challenging cross section which could hold multiple non-wetting regions. This cross section indicates two non-wetting regions, one in upper right and the other in lower left, compete with each other and our result shows the first region corresponds a larger r_e, thus this region is the final choice. Fig.29 also illustrates that the non-wetting region expands with the increasing of the wetting angle, which agree with the result in [17].

3.2 Average result

In the past researchers tried to predict the entry radius r_e by some basic geometry characters, and it is also one of the motivates of our research.

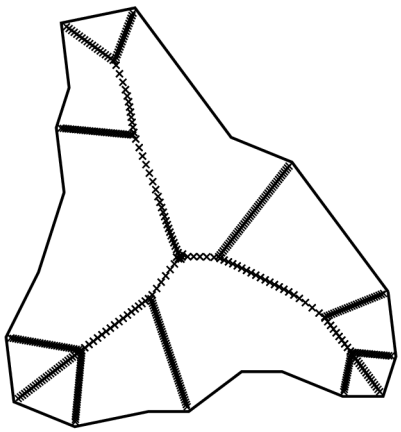

(a) $\theta = 0°$

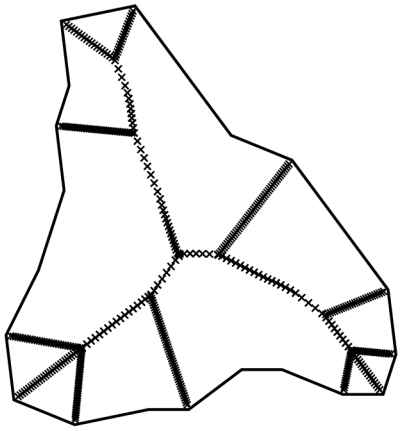

(b) $\theta = 10°$

Figure 28: Computed trajectories of menisci center, or drainage axis (DA) for different wetting angles.

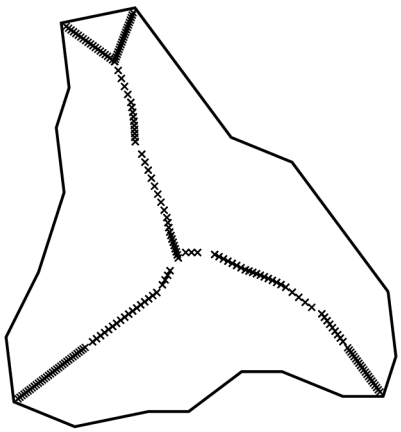

(c) $\theta = 20°$

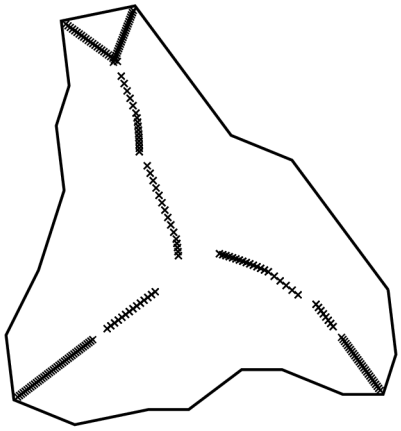

(d) $\theta = 30$

Figure 28: Computed trajectories of menisci center, or drainage axis (DA) for different wetting angles.

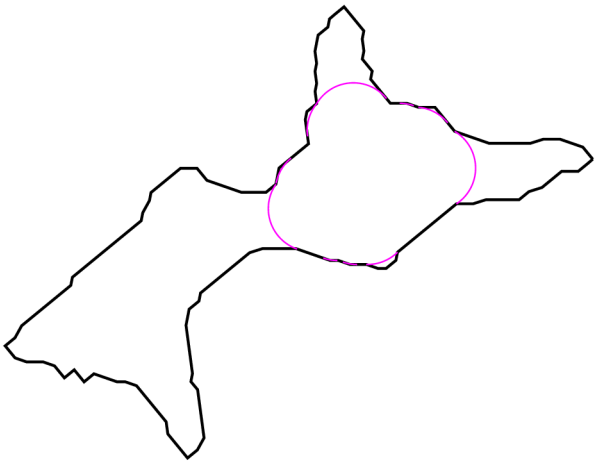

(a) $\theta = 0°$

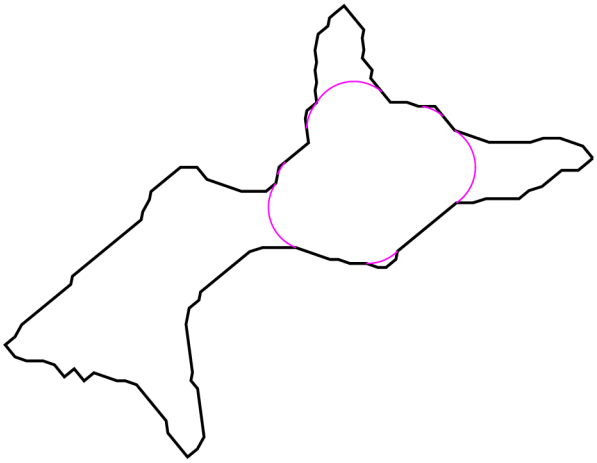

(b) $\theta = 10°$

Figure 29: The entry radii corresponding to different wetting angles.

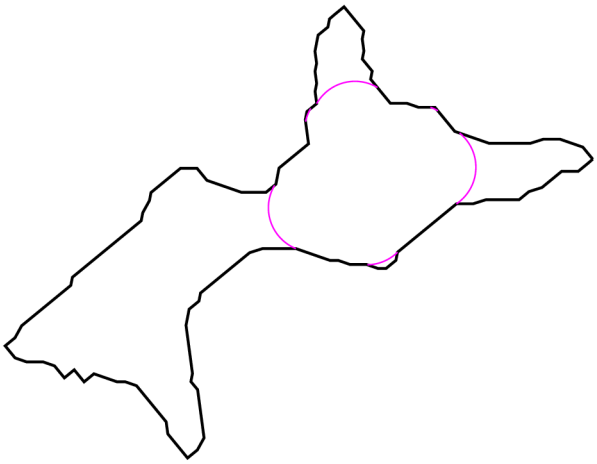

(c) $\theta = 20°$

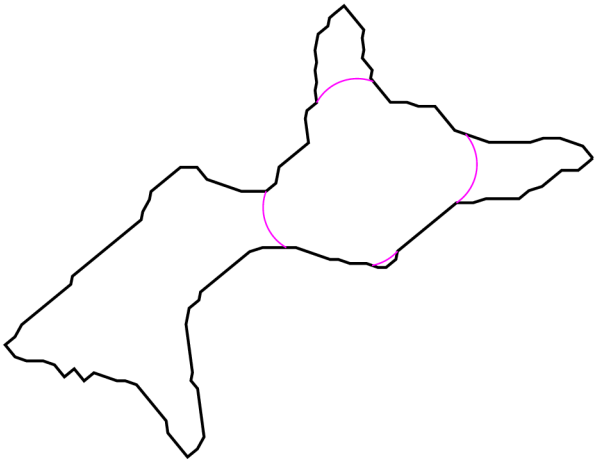

(d) $\theta = 30°$

Figure 29: The entry radii corresponding to different wetting angles.

Lindquist [36] has compared different candidates under the wetting angle $\theta = 0°$. Haines approximation [19], the largest radius of maximum inscribed circle, overestimates r_e more than 50%. Another candidate predictor $\sqrt{A/\pi}$, where A is the area of the cross section, is even worse. The hydraulic radius, proposed by Hwang [22], matches with r_e pretty well when $\theta = 0°$. Lindquist also noticed that the wetting angle θ has effect on r_e, however, lacking a tool to calculate r_e under $\theta > 0°$, he didn't explore the relation between r_e and θ further.

Later Frette and Helland [17] proposed a discretization method to calculate r_e under $\theta > 0°$, furthermore they suggested the the relation between r_e and θ should follow:

$$\frac{A/P}{r_e} = \frac{\cos\theta}{f(\theta)}. \tag{19}$$

Based upon a sample of 70 polygons, they estimated $f(0°) = 1.35$ and $f(40°) = 1.22$. Averaging over all polygons, our estimates for $f(\theta)$ are plotted in Fig.30. Our estimations are smaller than those obtained by Frette and Holland and more aligned with those presented in Kim and Lindquist [24]. And this plot indicates that $(A/P)\cos(\theta)$ provides a good estimation for the average entry radius within 5% error.

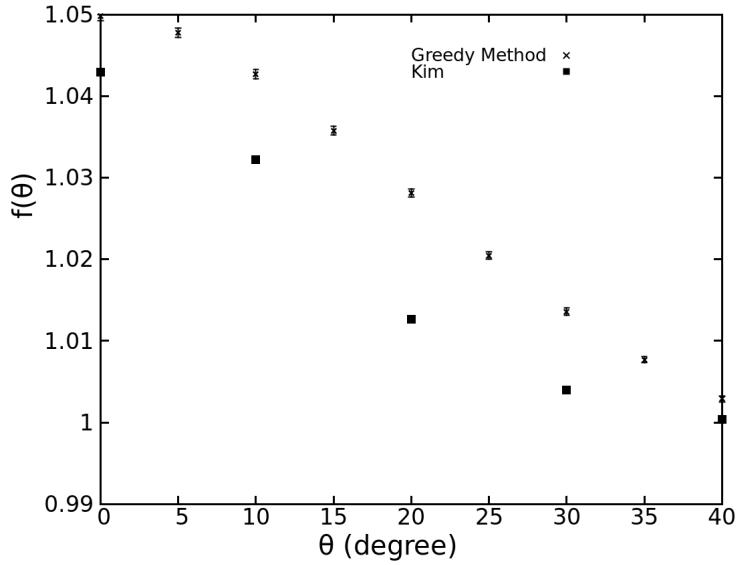

Figure 30: Comparison of our estimation of $f(\theta)$ with that of Kim *et al.* The error bars in our data represent 95% confidence intervals.

3.3 Effect of number of edges

The analytic expression for the entry radius for a regular polygon is [36]

$$r_e = \frac{A}{P} \cdot \frac{2}{\cos\theta + \sqrt{\cot\frac{\pi}{n} \cdot \left(\frac{\pi}{n} - \theta + \sin\theta\cos\theta\right)}} \quad \text{for } 3 \leq n \leq \frac{\pi}{\theta}\ , \qquad (20)$$

where A, P, and n refer respectively to the area, perimeter and number of edges of the polygon. The condition $n < \pi/\theta$ results from the requirement that the corners of the polygon support the presence of menisci. The behavior of the denominator of Eq.(20) suggests that the dimensionless ratio $(A/P)/r_e$

might have a general form

$$\frac{A/P}{r_e} = \cos\theta \cdot g(\theta, n) \ . \tag{21}$$

The analytic form of $g(\theta, n)$ for regular polygons can be computed from Eq.(20)

$$g_{\text{reg}}(\theta, n) = \frac{1}{2}\left\{1 + \left[\cot\frac{\pi}{n} \cdot \frac{\pi/n - \theta + \sin\theta\cos\theta}{\cos^2\theta}\right]^{1/2}\right\} \ . \tag{22}$$

$g_{\text{reg}}(\theta, n)$ is defined for $3 \leq n \leq \pi/\theta$ and has the property that $g_{\text{reg}}(\theta, \pi/\theta) = 1$. The first question we investigate is "how well does the form Eq.(21) predict the behavior of $(A/P)/r_e$ for actual throat polygons?". Fig.31 summarizes the data obtained from the sample of 23,639 throat polygons extracted from the imaged Fontainebleau sandstone sample. We plot mean value and 95% confidence intervals of $(A/P)/r_e$ measured from all polygons that have the same number of perimeter edges for 5 values of wetting angle θ. Also plotted (solid lines), for the same values of θ, are the functional forms Eq.(22).

We first note that, for a small number of edges, the measured behavior of $(A/P)/r_e$ tracks the behavior of $\cos(\theta) \cdot g_{\text{reg}}(\theta, n)$. Second, for $\theta = 40°$, for $n > \pi/\theta$, the behavior of $(A/P)/r_e$ is essentially constant at $(A/P)/r_e = \cos(\theta)$ (i.e. $g(\theta, n) = 1, ..., n > \pi/\theta$). For $\theta = 30°$, for $n > \pi/\theta$, the behavior of $(A/P)/r_e$ is also roughly constant, at approximately a value of $\cos(\theta)$. However, for $\theta = 20°$, $10°$ and $0°$, $(A/P)/r_e$ falls roughly linearly after reach-

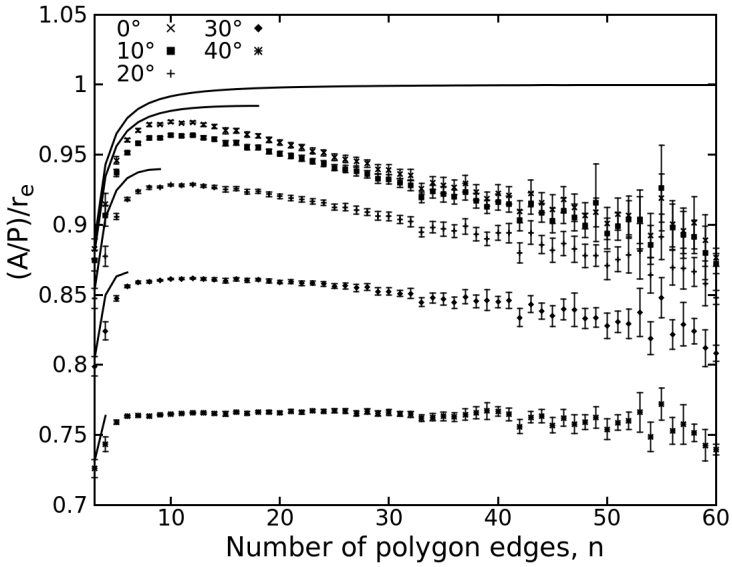

Figure 31: The behavior of $(A/P)/r_e$ (mean value and 95% confidence interval) as computed from throat polygons extracted from an image of a Fontainebleau sandstone sample polygons. Polygons with $n \geq 60$ edges are lumped together in this analysis. The data is compared against the behavior of $(A/P)/r_e$ for regular polygons (solid lines).

θ	$a(\theta)$ $(\times 10^{-3})$	$b(\theta)$
0°	-1.68	0.991
5°	-1.66	0.992
10°	-1.59	0.995
15°	-1.54	1.001
20°	-1.46	1.007
25°	-1.24	1.010
30°	-1.00	1.012
35°	-0.65	1.010
40°	-0.34	1.008

Table 6: Linear regression fits to the form (23).

ing a maximum value near $n = 10$. This decrease is most significant at the smaller wetting angles. To describe the measured data, we propose the form

$$g(\theta, n) = a(\theta) \cdot n + b(\theta) \tag{23}$$

for $g(\theta, n)$ in (21). Linear regression on the data for $n > 12$ in Fig.31, (including data for $\theta = 5^\circ$, 15°, 25° and 35° not displayed in Fig. 31) produces the results given in Table 6.

The table suggests a quadratic form for $a(\theta)$; regression returns the form

$$a = \left(3.5\ \theta^2 - 0.6\ \theta - 1.6\right) 10^{-3}, \tag{24}$$

where θ is the wetting angle in radians. The behavior of $b(\theta)$ is non-monotonic. The average and standard deviation for b over the measured range of angles

is 1.003 ± 0.008. Combining these observations, we suggest the form

$$g(\theta, n) = 1.0 + n \ \left(3.5\ \theta^2 - 0.6\ \theta - 1.6\right) 10^{-3} \ . \tag{25}$$

With $a(\theta)$ and $b(\theta)$ as given in Eq.(23), Fig.32 illustrates the quality of the fit of Eq.(23) to the measured data. Eq.(21) and Eq.(25) can be used to estimate the entry radius to an arbitrary polygon with n edges in a drainage process with wetting angle $0 \leq \theta < \pi/2$.

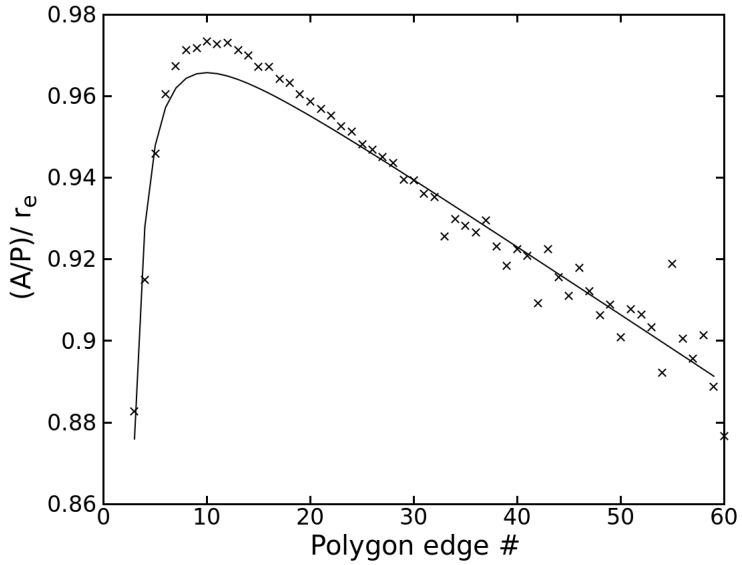

(a) $\theta = 0°$

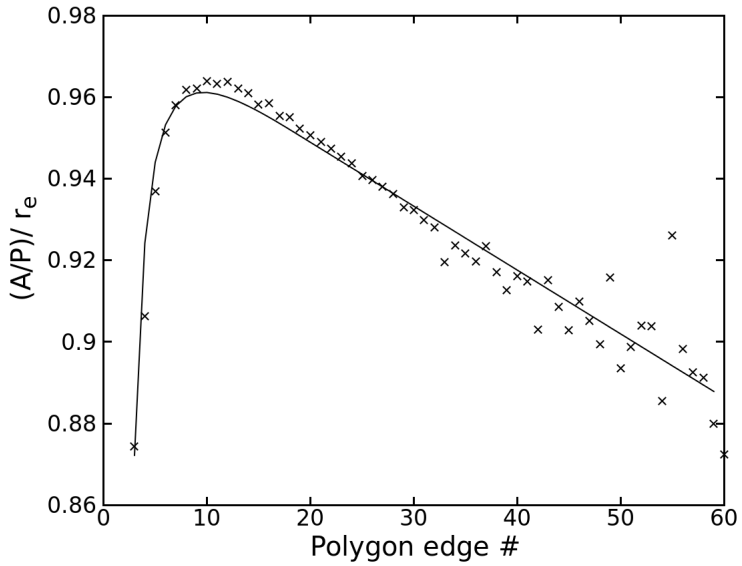

(b) $\theta = 10°$

Figure 32: Comparison of the analytic fits Eq.(21) and Eq.(25) to the data of Fig.31.

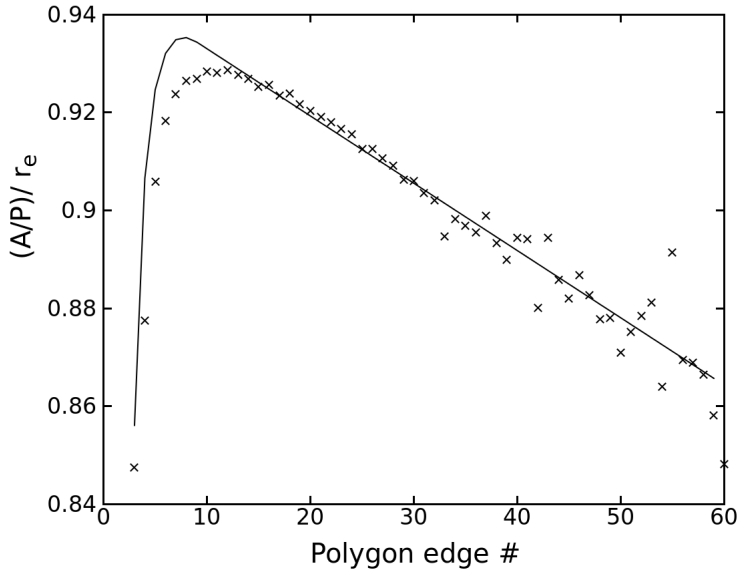

(c) $\theta = 20°$

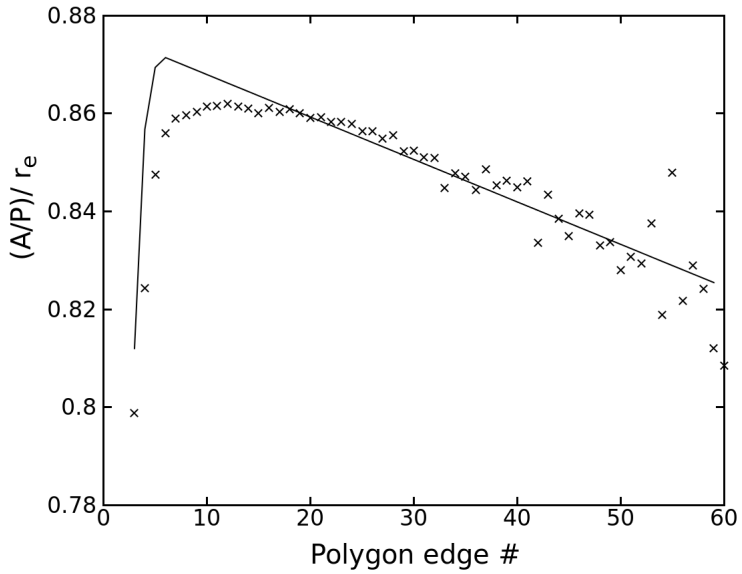

(d) $\theta = 30°$

Figure 32: Comparison of the analytic fits Eq.(21) and Eq.(25) to the data of Fig.31.

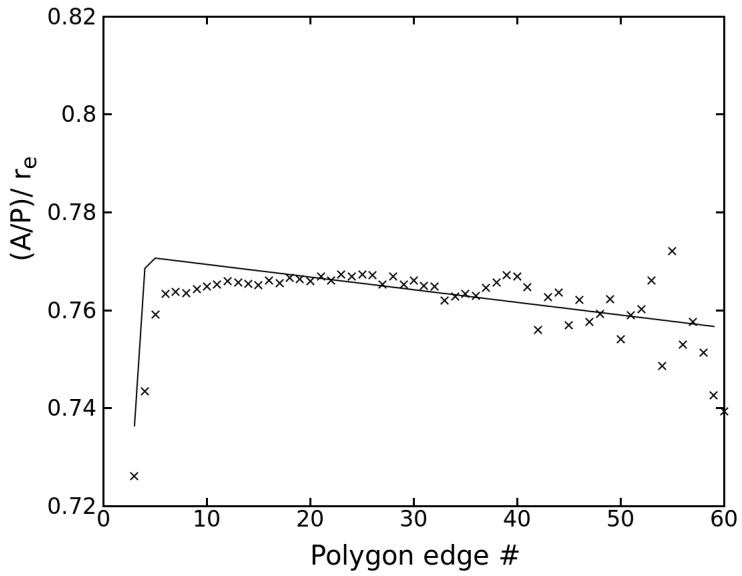

(e) $\theta = 40°$

Figure 32: Comparision of the analytic fits (21), (23), (24) to the data of Fig. 31.

4 Summary and discussion

We propose a new method to simulate the drainage process in a infinitely long capillary tube which may hold one or more possible non-wetting regions. The boundary of wetting and non-wetting fluid are menisci categorized into four different types (edge-edge, edge-vertex, vertex-edge, vertex-vertex) which we find are closely related with each other. With this inner logic relation we develop CC-circuits to represent individual non-wetting regions, then we get the entry radius of a cross section by comparing all entry radii of the corresponding CC-circuits. Utilizing this greedy method we can not only simulate the drainage process but also get the trace of drainage axis.

With the assistance of this method and 3DMA package we analyze 23,639 cross sections from Fontainebleau sample data, the result shows Eq.(21) and Eq.(25) could be employed to estimate entry radius r_e for any arbitrary single polygon with wetting angle θ less than $\pi/2$. Although $A/(P\cos\theta)$, or area over perimeter times cosine of the wetting angle, is a little coarser to predict r_e, it is still a good estimation of r_e for Fontainebleau sample data.

Moreover, the greedy method paves a road leading to some interesting topics in drainage process:

1. When the wetting angle θ is small, r_e is sensitive to edge numbers. And this sensitivity could be observed by the decline of the value $(A/P)/r_e$. Then the following question is raised naturally: what causes the decline? We guess the reason is the reflux vertices. As the more edges a polygon has, the more

reflux vertices it likely has. If that is true, it means the reflux vertices help to reduce the entry pressure to push a non-wetting fluid into a capillary tube which is occupied by another wetting fluid before. This conjecture needs a further exploration;

2. Our research object is an infinitely long capillary tube, it originates not only from what the Mayer-Stowe-Princen equation is based on, but also from the approximation that the radii of MA curve near throats are very large, or, channels don't swerve sharply near throats. The assumption is reasonable, however, the effects of MA curve radii are still unknown;

3. The greedy method can be applied to study the drainage process further beyond the entry status. It is quite easy to locate the corresponding menisci for the cross sections like Fig.2 which can hold only one single non-wetting region. However, for a cross section which may hold multiple non-wetting region, the situation could be more complex. With the increasing of the inlet pressure, the non-wetting regions appear one by one, therefore, it is unavoidable to consider the involvement between two neighbor menisci. For example, the M_2 and M_4 in Fig.23;

4. With proper revise, the greedy method could also be used to simulate imbibition process. In the greedy method, checking the partner list clockwise can guarantee the meniscus center falls onto the drainage axis in Fig.4. If we change the checking direction to counterclockwise, we could obtain a meniscus which agrees with the imbibition process. Meanwhile, the tests regarding to edge-vertex, vertex-edge and vertex-vertex need to be reexamined

and redesigned.

Appendix

Parallel Edge-edge Meniscus. We show that, if a meniscus spans two parallel edges, AB and DE (with the correct wetting angles), simultaneously translating its start and end points (maintaining wetting angle) along these edges produces no change in the value of the left-hand-side of Eq.(4). Consider the translation (Fig. 33) of meniscus M of radius r from start point F to G along AB (K to H on DE). The difference $\Delta f(r)$ of the left-hand-side of Eq.(4) when the meniscus is at position M' compared to when it was at position M is

$$\Delta f(r) = r\,\cos\theta\,[L_{FG} + L_{HK}] - A_{FGM'HKM}\ ,$$

where $L_{FG} \equiv |\overrightarrow{FG}| = |\overrightarrow{HK}| \equiv L_{HK}$ and $A_{FGM'HKM}$ is the area bounded by the straight segments FG and HK and the arcs M and M'. Noting that $A_{FGM'HKMF} = A_{FGHK}$ where A_{FGHK} is the rectangular area defined by those four points, $\Delta f(r)$ can be written

$$\begin{aligned}\Delta f(r) &= 2r\,\cos\theta\,L_{FG} - A_{FGHK}\\ &= L_{FK}L_{FG} - A_{FGHK}\\ &= 0\ .\end{aligned}$$

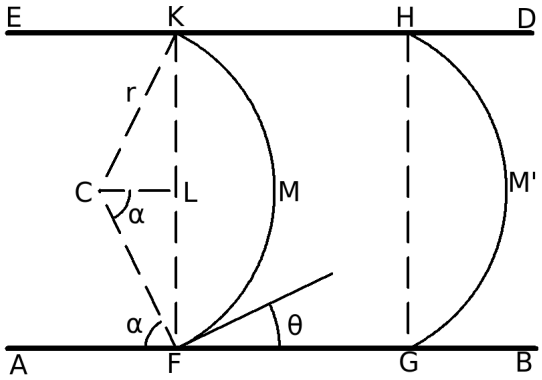

Figure 33: Parallel edge-edge meniscus should not exist when θ less than $\pi/2$.

References

[1] http://en.wikipedia.org/wiki/Porous_media

[2] Al-Dhahli A., van Dijke M.I.J., and Geiger S., Accurate modeling of pore-scale films and layers for three-phase flow processes in caustic and carbonate rocks with arbitrary wettability, Trans. Porous Media, 98 (2013), 259.

[3] Blum H. , A transformation for extracting new descriptors of shape, in Models for the Perception of Speech and Visual, W. Wathen-Dunn (Ed.), MIT Press, Cambridge, MA, 1967.

[4] Blunt M.J., Flow in porous media - pore-network models and multiphase flow, Curr. Opin. Colloid Interf. Sci., 6 (2001), 197.

[5] Brent R.P., Algorithms for Minimization without Derivatives, Englewood Cliffs, NJ: Prentice-Hall, 1973.

[6] Burdine N.T., Relative permeability calculation size distribution data, Pet. Trans. Am. Inst Min. Metal Pet. Eng., 198 (1953) 71

[7] Childs E.C., Collis-George N., The permeability of porous materials, Proc. Roy. Soc. Lond. A., 201 (1950) 392

[8] Cormen T.H., Leiserson C.E., Rivest R.L., Stein C., Introduction to algorithms, 2nd ed., Cambridge, Mass. : MIT Press, 2001

[9] Dias M. M., Payatakes A. C., Network models for two-phase flow in porous media part 1. immiscible microdisplacement of non-wetting fluids, J. Fluid Mech., 164 (1986) 305.

[10] Dias M. M., Payatakes A. C., Network models for two-phase flow in porous media part 2. motion of oil ganglia, J. Fluid Mech., 164 (1986) 337.

[11] Fatt I. , The network model of porous media: I. Capillary pressure characteristics, Trans. Am. Inst. Min. Metall. Eng., 207 (1956) 144.

[12] Fatt I., The network model of porous media, II, Dynamic properties of a single size tube network, Trans. Am. Inst. Min. Metall. Pet. Eng., 207 (1956) 160

[13] Fatt I., The network model of porous media, III, Dynamic properties of networks with tube radius distribution, Trans. Am. Inst. Min. Metall. Pet. Eng., 207 (1956) 164

[14] Fenwick D.H., Blunt M.J., Three-dimensional modeling of three-phase imbibition and drainage. Adv Water Resour 25 (1998) 121

[15] Fenwick D.H., Blunt M.J., Network modeling of three-phase flow in porous media. SPE J 3 (1998) 86

[16] Flannery B.P., Deckman H.W., Roberge W.G., D'Amico K.L., Three-dimensional X-ray microtomography, Science, 237 (1987) 1439.

[17] Frette O.I., Helland J.O., A semi-analytical model for computation of capillary entry pressures and fluid configurations in uniformly-wet pore spaces from 2D rock images, Adv. Water Resour. 33 (2010) 846.

[18] Glantz R., Hilpert M., Capillary displacement in totally wetting and infinitely long right prisms, Multiscale Model. Simul. 9 (2011) 1765.

[19] Haines W.B., Studies in the physical properties of soils: IV. A further contribution to the theory of capillary phenomena in soil, J. Agr. Sci. 17 (1927) 264.

[20] Held M. , Analytical computation of arc menisci configuration under primary drainage in convex capillary cross sections, Comput. Geosci. 14 (2010) 311.

[21] Helland J.O., Frette O.I., Computation of fluid configurations and capillary pressures in mixed-wet 2D pore spaces from rock images, Computational Methods in Water Resources XVIII International Conference, 2010, Barcelona, Spain.

[22] Hwang S.T. , The Gauss equation in capillarity, Z. Physik. Chemie Neue Folge, 105 (1977) 225.

[23] Kinney, J.H., Nichols M.C., X-ray tomographic microscopy (XTM) using synchrotron radiation, Annu. Rev. Mater. Sci., 22 (1992) 121.

[24] Kim D., Lindquist W.B. , A semianalytic model for the computation of imbibition through polygonal cross sections, Water Resour. Res. 48 (2012) W04529

[25] Koplik J., Lasseter T. J., Two-phase flow in random network models of porous media, SPEJ, 25 (1985) 89.

[26] Koplik J., Creeping flow in two-dimensional networks. J. Fluid Mech 119 (1982) 219.

[27] Kovscek A.R., Wong H., Radke C.J., A pore-level scenario for the development of mixed wettability in oil reservoirs, Am. Inst. Chem. Eng. J. 39 (1993) 1072.

[28] Lago M., Araujo M., Threshold pressure in capillaries with polygonal cross section, J. Colloid Interf. Sci. 243 (2001) 219.

[29] Lee T.C., Kashyap R.L., Chu C.N., Building skeleton models via 3-D medial surface/axis thinning algorithms, CVGIP: Graph. Models Image Proc. 56 (1994) 462.

[30] Lenormand R., Zarcone C., Sarr A., Mechanisms of the displacement of one fluid by another in a network of capillary ducts, J. Fluid Mech. 135 (1983) 337.

[31] Lindquist, W.B., Lee S.M., Coker D.A., Jones K.W., Spanne P., Medial axis analysis of three dimensional tomographic images of drill core samples, J. Geophys. Res., 101B (1996) 8297.

[32] Lindquist W. B., Venkatarangan A., Dunsmuir J., Wong T. F., Pore and throat size distributions measured from synchrotron X-ray tomographic images of Fontainebleau sandstones, J. Geophys. Res. 105 (2005) 21508.

[33] Lindquist W.B. and Venkatarangan A. , Investigating 3D geometry of porous media from high resolution images, Phys. Chem. Earth, A 24 (1999) 593.

[34] Lindquist W.B., 3DMA-Rock: A software package for automated analysis of rock pore structure in 3D computed microtography images. http://www.ams.sunysb.edu/~lindquis/3dma/3dma_rock/3dma_rock.html

[35] Lindquist W.B., Quantitative analysis of three-dimensional X-ray tomographic images, Proc. SPIE 4503, (2002) Developments in X-Ray Tomography III, 103.

[36] Lindquist W.B., The geometry of primary drainage, J. Colloid Interf. Sci. 296 (2006) 655.

[37] Ma S., Mason G., Morrow N.R., Effect of contact angle on drainage and imbibition in regular polygonal tubes, Colloids Surf. A 117 (1996) 273.

[38] Man H.N., Jing X.D., Network modeling of wettability and pore geometry effects on electrical resistivity and capillary pressure. J Petroleum Sci Eng 24 (1999) 255.

[39] Man H.N., Jing X.D., Pore network modeling of electrical resistivity and capillary pressure characteristics. Transp Porous Media 41 (2000) 263.

[40] Man H.N., Jing XD. Network modeling of strong and intermediate wettability on electrical resistivity and capillary pressure. Adv Water Resour 24 (2001) 345.

[41] Mason G., Morrow N.R., Capillary behavior of a perfectly wetting liquid in irregular triangular tubes, J. Colloid Interf. Sci. 141 (1991) 262

[42] Mayer R.P., Stowe R.A., Mercury porosimetry — breakthrough pressure for penetration between packed spheres, J. Colloid Interf. Sci. 20 (1965) 893.

[43] Oh W., Lindquist W. B., Image thresholding by indicator kriging, IEEE Trans. Pattern Anal. Mach. Intel. 21 (1999) 590.

[44] ren P.E., Bakke S. , Arntzen O.J., Extending predictive capabilities to network models, SPEJ. 3 (1998) 324.

[45] O'Rourke J., Computational Geometry in C, 2nd edtion , Cambridge University Press, 1998

[46] Princen H.M., Capillary phenomena in assemblies of parallel cylinders. I. Capillary rise between two cylinders, J. Colloid Interf. Sci. 30 (1) (1969) 69.

[47] Princen H.M., Capillary phenomena in assemblies of parallel cylinders. II. Capillary rise in systems with more than two cylinders, J. Colloid Interf. Sci. 30 (3) (1969) 359.

[48] Princen H.M., Capillary phenomena in assemblies of parallel cylinders. III. Liquid columns between horizontal parallel cylinders, J. Colloid Interf. Sci. 34(2) (1970) 171.

[49] Prodanovic M., Lindquist W.B., Seright R.S., Porous structure and fluid partitioning in polyethylene cores from 3D X-ray microtomographic imaging, J. Colloid Interf. Sci. 298 (2006) 282.

[50] Shin H., Lindquist W.B. , Sahagian D.L., Song S.R., Analysis of the vesicular structure of basalts, Comput. Geosci. 31 (2005) 473.

[51] Thovert, J.F., Salles J., Adler P.M., Computerized characterization of the geometry of real porous media: Their discretization, analysis and interpretation, J. Microsc., 170 (1993) 65.

[52] van Dijke, M.I.J., Sorbie K.S., Existence of fluid layers in the corners of a capillary with non-uniform wettability, J. Colloid Interf. Sci., 293 (2006) 455.